Energy Storage Materials 51 (2022) 38–53

Contents lists available at ScienceDirect

Energy Storage Materials

journal homepage: www.elsevier.com/locate/ensm

Ternary chalcogenide anodes for high-performance potassium-ion batteries and hybrid capacitors via composition-mediated bond softening and intermediate phase

Wei-Cheng Lin, Yi-Chun Yang, Hsing-Yu Tuan *

Department of Chemical Engineering, National Tsing Hua University, Hsinchu 30013, Taiwan

ARTICLE INFO

Keywords:
Potassium
Chalcogenide
Batteries
Capacitors
Composition

ABSTRACT

Despite the high potassium-ion storage of chalcogenide anodes relative to intercalation-based graphite, inhibition of their large volume change during the potassiation/depotassiation process, and stabilization of reversible electrochemical reactions to ensure efficient electron/ion transfer remain challenging. Here we report composition-tunable ternary chalcogenides that achieve highly reversible potassium-ion storage through synergistic interactions between elements. A series of $Bi_{2-x}Sb_xSe_3$ ternary chalcogenide (x = 0, 0.25, 1, 1.75, 2) solid solutions with a full composition range are designed using a facile high energy mechanical milling method. Sb_2Se_3 substituted by Bi gives rise to a chemical bond softening effect that accompanies structural transition and maintains excellent structural stability. Meanwhile, the intermediate quaternary-phase $K_3(Bi,Sb)Se_3$ enables a highly reversible 12-electron transfer conversion/alloying reaction during the potassiation/depotassiation process. Various electrochemical analyses show that $Bi_{2-x}Sb_xSe_3$ inherits the advantages of binary Sb_2Se_3 (high capacity) and Bi_2Se_3 (stability) while balancing their respective disadvantages, confirming the synergistic effect of ternary chalcogenide systems. By engineering $Bi_{2-x}Sb_xSe_3$ implemented into potassium-ion based full cells, we demonstrate a high energy/power density of 76.9 W h kg^{-1}/1964.2 W kg^{-1} for batteries and 54.3 W h kg^{-1}/3685.7 W kg^{-1} for hybrid capacitors. This work illustrates how to exploit the underlying multilateral science and the relevant electrochemistry of ternary chalcogenides to achieve excellent electrochemical performance, suggesting a new avenue of anode design for potassium-ion storage.

1. Introduction

Lithium-ion batteries and supercapacitors are two typical examples of electrical energy storage. It is well known that lithium-ion batteries have high energy density but suffer from low power density and poor cycling performance. On the other hand, lithium-ion supercapacitors have high power density and long cycle life. However, the scarcity of lithium resources (0.0017%), high cost, and the serious safety issues brought about by lithium dendrites may not meet the needs of growing large-scale applications [1,2]. Therefore, the development of alternative and sustainable battery systems based on Earth-rich metals, such as Na, K, Mg, and Zn is indispensable [3–5]. Among these metals, potassium-ion energy storage has the following advantages due to an energy storage mechanism similar to Li^+ components: (1) the redox potential of K^+ (−2.93 V vs. SHE) is close to that of Li^+ (−3.04 V vs. SHE), implying a high voltage platform and energy density; (2) K^+ has higher ionic mobility and ionic conductivity because its Stokes radius (3.6 Å) in propylene carbonate solvent is smaller than that of Li; (3) it is considered a low-cost and sustainable system due to its lower electrolyte price (*e.g.*, KPF_6 is 20 times cheaper than $LiPF_6$) [6–8].

Chalcogenides, such as sulfides (*e.g.*, SnS, Bi_2S_3, and Sb_2S_3) and selenides (*e.g.*, SnSe, Bi_2Se_3, and Sb_2Se_3), for potassium-ion anodes have attracted attention because they simultaneously undergo conversion and alloying reactions to achieve higher theoretical capacities relative to intercalation-based anodes, such as graphite [9–14]. Selenide systems have higher electronic conductivity compared with metal sulfides due to the high conductivity of Se (1×10^{-3} S m^{-1}), which is higher than S (5×10^{-28} S m^{-1}), suggesting lower energy barriers for ion diffusion than those in oxides and sulfides. Although the gravimetric capacity of Se (679 mA h g^{-1}) is lower than that of S (1,675 mA h g^{-1}), the volumetric capacity of Se (3,250 mA h cm^{-3}) is comparable to that of S (3,470 mA h cm^{-3}) due to the density of Se (4.8 g cm^{-3}) being higher than that of S

* Corresponding author.
E-mail address: hytuan@che.nthu.edu.tw (H.-Y. Tuan).

https://doi.org/10.1016/j.ensm.2022.06.010
Received 17 March 2022; Received in revised form 27 May 2022; Accepted 8 June 2022
Available online 16 June 2022

(1.8 g cm^{-3}) [15]. Unfortunately, the large volume change of the selenide electrode during the potassiation/depotassiation process will cause severe pulverization and rapid capacity fading [16]. Therefore, the suppression of pulverization is of great significance for improving the reversibility of K^+ transfer while pursuing the durable performance of Sb_2Se_3 anodes. Methods such as carbon modification ($MoSe_2$, $FeSe_2$, $CoSe_2$, V_5Se_8, *etc.*), microstructure optimization (VSe_2 and CuSe, etc.), doping engineering (e.g., Cu-doped $CoSe_2$ and Co-doped FeS_2 nanospheres), and multi-element combination (e. g., CoPSe/C and Bi_2O_2Se) have been developed to improve the electrochemistry of chalcogenide-based potassium-ion electrodes [17–26]. However, the application of the underlying multilateral science remains unclear.

Ternary compounds have attracted much attention relative to binary compounds because the introduction of a third element enables a synergistic effect between the various components to generate new attractive properties or functions. The electrochemical performance of binary or ternary original materials can be improved by tailoring the solid solution composition. For example, a solid solution makes $FeS_{2-x}Se_x$ capable of combining the high specific capacity of FeS_2 with the good redox kinetics of $FeSe_2$, thereby exhibiting an ultra-long cycle life and superior rate capability. Based on the DOS results, mesophase $Na_2FeS_{2-x}Se_x$ produced by sodiation is beneficial to carrier transportation and improves conductivity [27]. Yokozaki et al. reported that an Al-substituted $MgMn_{2-x}Al_xO_4$ solid solution has better cathode performance than undoped $MgMn_2O_4$ [28]. Bhatia et al. later reported that solid electrolyte $La_{1-x}Ba_xF_{3-x}$ ($0 \leq x \leq 0.15$) with a Tysonite structure was produced through wet chemical synthesis. Compared with a ball-milled electrolyte, the battery using the $La_{0.95}Ba_{0.05}F_{2.95}$ electrolyte exhibited excellent performance, high discharge capacity and capacity retention, and smaller hysteresis [29]. Konishi et al. showed that BiF_3–BaF_2 solid solutions with various crystal structures can be obtained using the mechanical alloying method. In the charge/discharge curves, the capacity retention rate of $Bi_{1-x}Ba_xF_{3-x}$ ($x = 0$, 0.2, 0.4) is improved with increasing barium content [30]. b-$K_2Bi_8Se_{13}$ has been alloyed with its isostructural $K_2Sb_8Se_{13}$ analog to produce $K_2(Bi_{1-z}Sb_z)_8Se_{13}$. The resulting Bi/Sb substitution in the structure produced a wide range of quality fluctuations in the crystal lattice of $K_2Bi_8Se_{13}$ [31]. Wang et al. reported the K^+-insertion process of Sb_2MoO_6 via operando XRD, TEM, density functional theory (DFT) calculation and deduced that the Sb element is mainly responsible for the high capacity, while Mo improves conductivity and cycle performance by forming an amorphous matrix. Therefore, the Sb_2MoO_6/rGO electrode delivered a discharge capacity of 247 mA h g^{-1} after 100 cycles at 500 mA g^{-1} with a high Columbic efficiency [32].

Here, we design a series of $Bi_{2-x}Sb_xSe_3$ ternary chalcogenides ($x = 0$, 0.25, 1, 1.75, 2) as anodes for a potassium-ion battery (PIB) and a potassium-ion hybrid capacitor (PIHC) with high performance. As shown in Scheme 1, $Bi_{2-x}Sb_xSe_3$ with controllable composition and structure was synthesized by a simple high energy mechanical milling method. Since Sb and Bi have the same crystal structure, which can form a $Bi_{2-x}Sb_xSe_3$ solid solution, the composition can be systematically tuned over a wide range. The following two advantages of $BiSbSe_3$ anodes allow highly reversible potassium-ion storage: (1) Bi/Sb composition-induced chemical bond softening can reduce the effect of volume expansion/contraction during cycling, which shows outstanding structure stability [33], and (2) the intermediate quaternary-phase $K_3(Bi,Sb)Se_3$ observed during the potassiation/depotassiation process promotes a reversible conversion/alloying reaction based on 12-electron transfer. Finally, a PIB with a Prussian blue (PB) cathode and a PIHC with an activated carbon (AC) cathode were fabricated to evaluate the feasibility of $BiSbSe_3$ anodes in advanced storage systems. The fabricated PIB and PIHC exhibited high energy/power density values of 76.9 W h kg^{-1}/1964.2 W kg^{-1} and 54.3 W h kg^{-1}/3685.7 W kg^{-1} for, respectively.

2. Results and discussion

$Bi_{2-x}Sb_xSe_3$ was synthesized via a simple high energy mechanical grinding method schematically illustrated in Fig. 1a. Based on the Bi_2Se_3–Sb_2Se_3 phase diagram (Fig. S1), $Bi_{2-x}Sb_xSe_3$ is rhombohedral phase (Bi_2Se_3-based) when $x \leq 0.26$, pure orthorhombic phase (Sb_2Se_3-based) when $x \geq 1.0$, and mixed crystal phases are present when $0.26 < x < 1.0$. Fig. 1b presents the crystal structures of five samples ($Bi_{2-x}Sb_xSe_3$; $x = 0$, 0.25, 1, 1.75, 2) corresponding to the phase diagram. Fig. 1c shows the XRD pattern of the synthesized $Bi_{2-x}Sb_xSe_3$ ($x = 0$, 0.25, 1, 1.75, 2) with the diffraction peaks of the XRD pattern indexed to the rhombohedral crystal structure of the Bi_2Se_3 phase (PDF 00-033-0214) or the orthorhombic crystal structure of the Sb_2Se_3 phase (PDF 01-083-7429). When x is increased to one, all rhombohedral Bi_2Se_3 phase peaks disappear and only the orthorhombic Sb_2Se_3 phase can be indexed, indicating that the $Bi_{2-x}Sb_xSe_3$ has the orthorhombic crystal structure of Bi-doped Sb_2Se_3. It can be concluded that $Bi_{2-x}Sb_xSe_3$ has the rhombohedral crystal structure of Sb-doped Bi_2Se_3 in the lower Sb content range of $x = 0$–1, and the orthorhombic crystal structure of Bi-doped Sb_2Se_3 while in a Sb content range of $x = 1$–2. Due to the high Bi content in $Bi_{2-x}Sb_xSe_3$ with a rhombohedral crystal system, the a-axis of the crystal structure is shorter and the c-axis is longer than when $x = 0$ due to a small amount of Sb incorporation, resulting in an increase in c/a but decrease in cell volume. The decrease in cell volume is mainly due to the replacement of the smaller Sb (covalent radii rSb = 1.38 Å and rBi = 1.46 Å). More importantly, the significant structural changes during the phase transition will cause significant changes in the

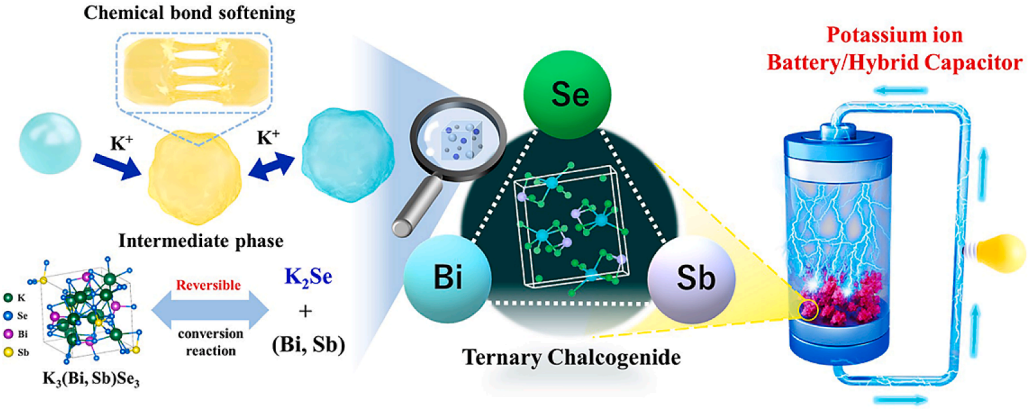

Scheme 1. Ternary chalcogenide anode ($Bi_{2-x}Sb_xSe_3$) as an anode for high power density/energy density of PIBs and PIHCs, and two key factors affecting their high electrochemical performance as follows: (1) chemical bond softening suppresses potassiation-induced volume expansion and pulverization; (2) the formation of intermediate quaternary-phase $K_3(Bi,Sb)Se_3$ enables a better reversibility of the conversion/alloying reaction.

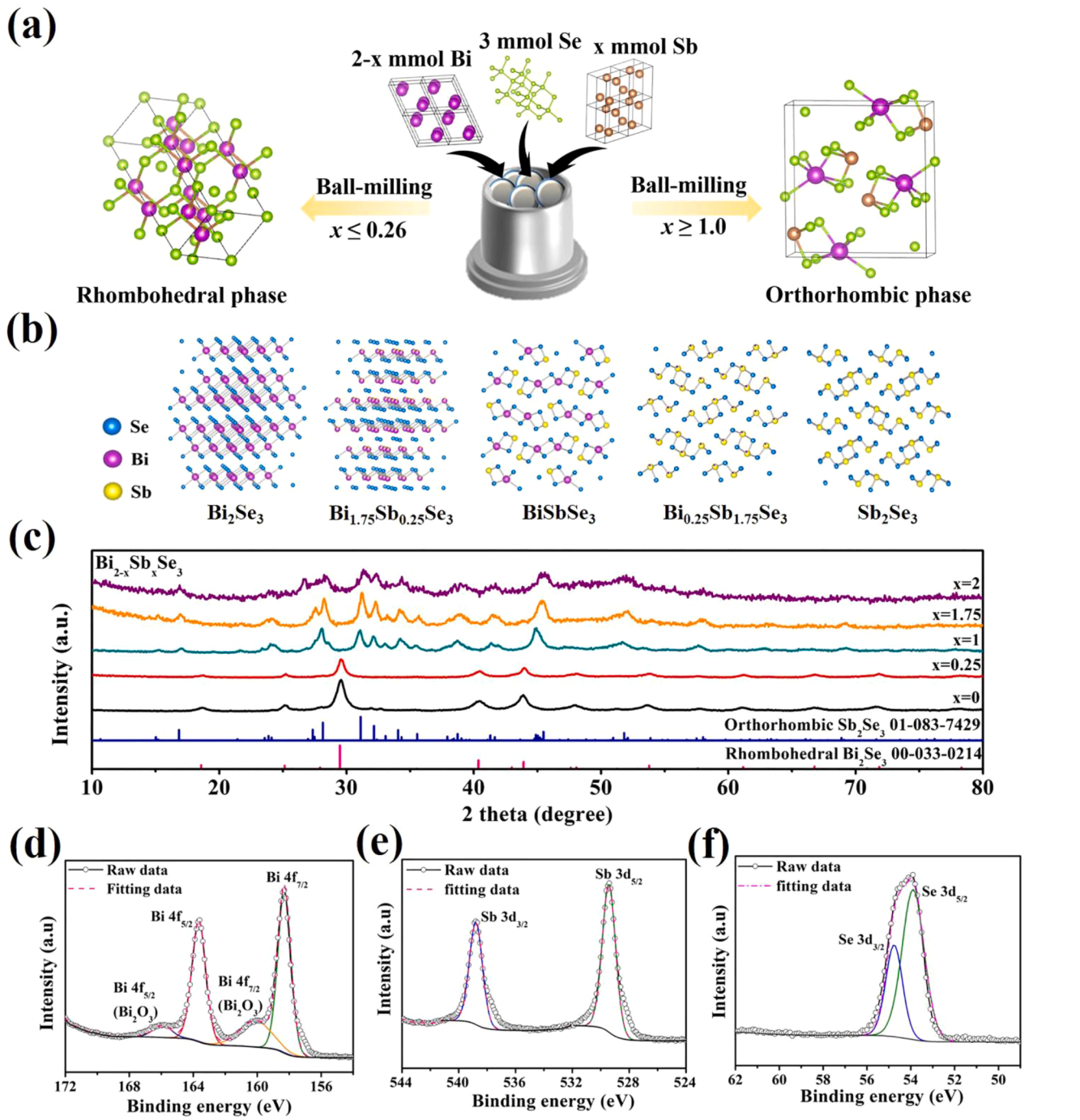

Fig. 1. (a) Schematic illustration of $Bi_{2-x}Sb_xSe_3$ alloys, synthesized by a simple high-energy mechanical milling method and the Bi/Sb composition-induced structural transition ($Bi_{2-x}Sb_xSe_3$ is a rhombohedral phase when $x \leq 0.26$ and a pure orthorhombic phase exists when $x \geq 1.0$). (b) Crystal structures and (c) XRD patterns of $Bi_{2-x}Sb_xSe_3$ alloys. (d) High-resolution XPS spectra of (d) Bi 4f, (e) Sb 3d, and (f) Se 3d for $BiSbSe_3$.

electronic band structure and lattice dynamics, thereby adjusting the electrochemical properties of the $Bi_{2-x}Sb_xSe_3$ [34]. Fig. 1d–f and S2–4 show the chemical state of elements on the surfaces of $BiSbSe_3$ and $BiSbSe_3$ containing graphite, which was investigated by X-ray photoelectron spectroscopy (XPS) spectrum and indicated that the presence of Bi, Sb, and Se. The deconvoluted Bi spectrum (Fig. 1d) has four peaks, with positions corresponding to 164 and 158 eV assigned to Bi $4f_{5/2}$ and Bi $4f_{7/2}$, respectively. The other two peaks in Fig. 1d can be classified as Bi oxidation (Bi_2O_3 $4f_{5/2}$ and Bi_2O_3 $4f_{7/2}$) [35]. However, no oxide was detected by the XRD measurements, suggesting that the Bi_2O_3 signals are only surface oxides. As shown in Fig. 1e, the two peaks at 539 and 530 eV are assigned to Sb $3d_{3/2}$ and Sb $3d_{5/2}$ [36], respectively. There are also peaks of Se $3d_{3/2}$ and Se $3d_{5/2}$ located at 55.5 and 53.5 eV, respectively (Fig. 1f) [11].

As shown in Figs. 2 and S5, the detailed microstructures of $Bi_{2-x}Sb_xSe_3$ ($x = 0.25, 1, 1.75$) and $BiSbSe_3$ mixed with graphite were imaged via scanning electron microscopy (SEM), transmission electron microscope (TEM), elected area diffraction (SAED), and high-resolution TEM (HRTEM). In Fig. 2a–c and S5a, SEM images displayed the morphology of the as-prepared $Bi_{2-x}Sb_xSe_3$ ($x = 0.25, 1, 1.75$) and $BiSbSe_3$ mixed with graphite shows similar irregular shapes and feature sizes ranging from 500 to 1000 nm. Figs. 2d–f and S8b are TEM images of $Bi_{2-x}Sb_xSe_3$ with $x = 0.25, 1, 1.75$, respectively, and $BiSbSe_3$ mixed with graphite at low magnification. All x values show irregular

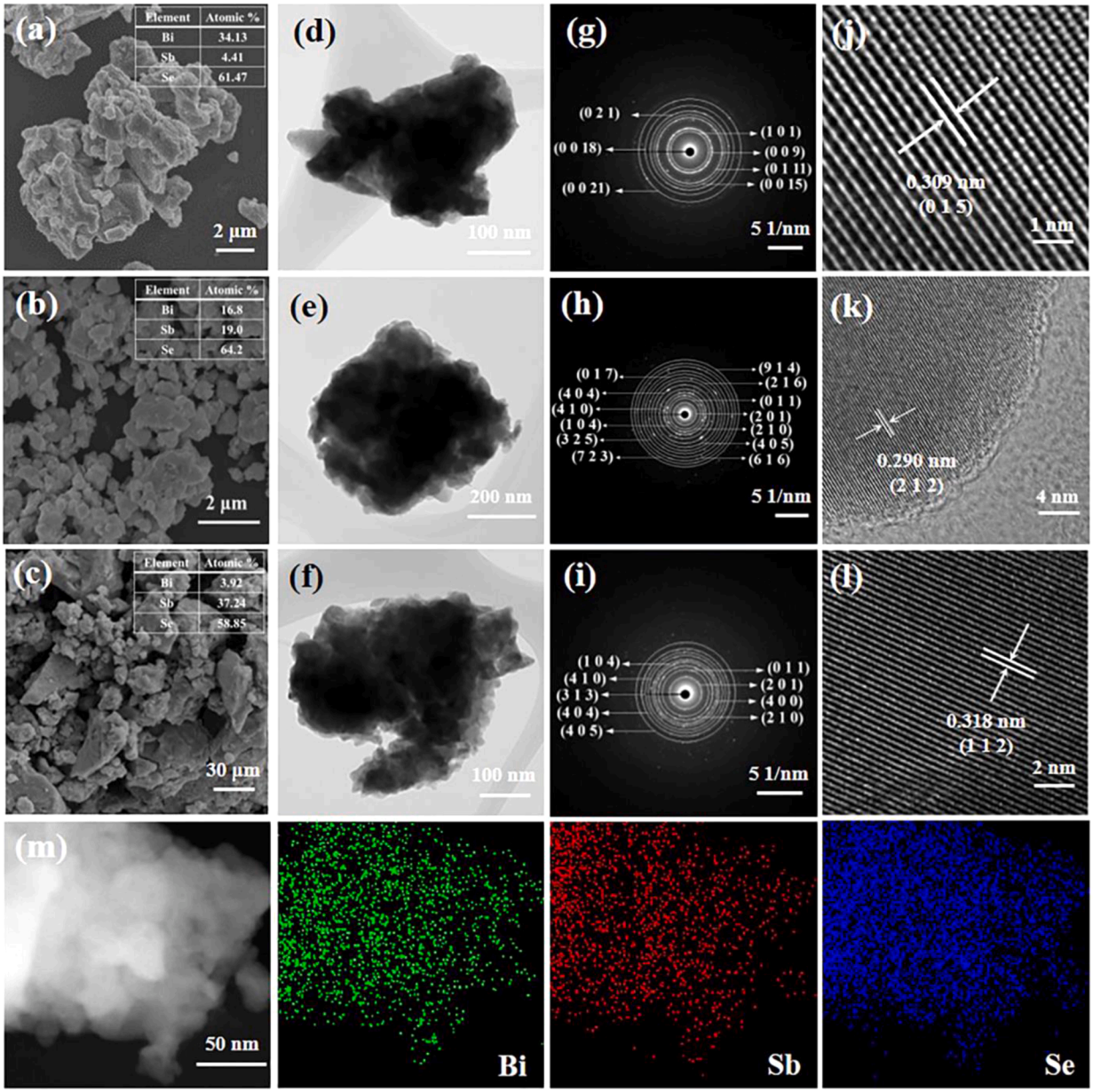

Fig. 2. (a–c) SEM, (d–f) TEM, (g-i) SAED and (j-l) HRTEM images of $Bi_{1.75}Sb_{0.25}Se_3$, $BiSbSe_3$ and $Bi_{0.25}Sb_{1.75}Se_3$. (m) EDS mapping images of $BiSbSe_3$ and corresponding elements of Bi, Sb and Se.

morphology. However, it can be observed that $BiSbSe_3$ is uniformly encapsulated in flake graphite in Fig. S5b. However, differences between the $Bi_{2-x}Sb_xSe_3$ materials were observed by SAED (Fig. 2g–i), even though they are similar in appearance. First, the SAED patterns of $Bi_{1.75}Sb_{0.25}Se_3$ are significantly different from those of $BiSbSe_3$ and $Bi_{0.25}Sb_{1.75}Se_3$. The SAED patterns of $Bi_{1.75}Sb_{0.25}Se_3$ are assigned to the (1 0 1), (0 0 9), (0 1 11), (0 0 15), (0 2 1), (0 0 18), and (0 0 21) planes of the rhombohedral phase of $Bi_{1.75}Sb_{0.25}Se_3$. In contrast, the SAED patterns of $BiSbSe_3$ and $Bi_{0.25}Sb_{1.75}Se_3$ were similar. The SAED patterns of $BiSbSe_3$ and $Bi_{0.25}Sb_{1.75}Se_3$ are assigned to the (2 0 1), (0 1 1), (2 1 0), (1 0 4), (4 1 0), (4 0 4), and (4 0 5) planes of the orthorhombic phases of $BiSbSe_3$ and $Bi_{0.25}Sb_{1.75}Se_3$. Additionally, the SAED pattern of $BiSbSe_3$ mixed with graphite is shown in Fig. S5c, which clearly reveals that the composites have two different crystalline phases: $BiSbSe_3$ and graphite. The HRTEM analysis results are similar to those of SAED. The HRTEM image for $Bi_{1.75}Sb_{0.25}Se_3$ shows lattice fringes of 0.309 nm, which is consistent with the (0 1 5) plane of rhombohedral phase of $Bi_{1.75}Sb_{0.25}Se_3$ (Fig. 2j). Moreover, the HRTEM images of $BiSbSe_3$ and $Bi_{0.25}Sb_{1.75}Se_3$ indicate that the lattice fringe spaces of 0.290 and 0.318 nm, which are assigned to the (2 1 2) plane of $BiSbSe_3$ and the (1 1 2) plane of $Bi_{0.25}Sb_{1.75}Se_3$, respectively (Fig. 2k and l). The HRTEM image of $BiSbSe_3$ mixed with graphite demonstrated two distinct lattice fringes with d-spacing of 0.284 nm and 0.336 nm, respectively (Fig. S5d), which were assigned to (2 1 2) plane of $BiSbSe_3$ and (0 0 2) plane of graphite. Fig. 2m shows scanning TEM energy dispersive spectroscopy (STEM-EDS) element mapping analysis of $BiSbSe_3$, which indicates good distribution of Bi, Sb, and Se elements. STEM-EDS analysis shows that the molar ratio of Bi/Sb/Se is close to 17:19:64, which is consistent with the designed composition. And, the STEM and EDS mapping images of $BiSbSe_3$ mixed with graphite shown in Fig. S5e suggest successful synthesis of $BiSbSe_3$ mixed with graphite composite with Bi, Sb and Se elements distributing homogeneously on the particle structure inside and C distributing homogeneously on the flake structure outside. Figs. S6–8 show the STEM-EDS analyses of $Bi_{1.75}Sb_{0.25}Se_3$, $Bi_{0.25}Sb_{1.75}Se_3$, Bi_2Se_3 and Sb_2Se_3. In addition, the detailed microstructures of $BiSbSe_3$ after mixing with graphite to improve its conductivity were also explored by

XRD, Raman spectroscopy and thermogravimetric analysis (TGA), which indicate that carbon is uniformly distributed outside $BiSbSe_3$ (Figs. S9–11). Fig. S9 showed the XRD patterns of $BiSbSe_3$ and $BiSbSe_3$ mixed with graphite. Compared with the $BiSbSe_3$ raw material, the XRD pattern peak intensity of $BiSbSe_3$ mixed with graphite was reduced, but it also showed the same diffraction peak position, and an additional peak appears between 26° and 27°, which corresponds to (0 0 2) plane of graphite. The degree of graphitization of the composite material could be analyzed by Raman spectroscopy. As shown in Fig. S10, the Raman spectrum of $BiSbSe_3$ mixed with graphite could observe two peaks at 1351 cm^{-1} and 1580 cm^{-1}, attributed to disordered carbon (D-band) and ordered carbon (G-band), respectively. These two bands could reflect the number of structural defects and the degree of the graphitization [37]. The result showed that the structure of graphite became more disordered after ball-milling process. The TGA curve was shown in Fig. S11, the exact carbon content for $BiSbSe_3$ containing graphite can be calculated as 33%.

The reaction mechanism of $Bi_{2-x}Sb_xSe_3$ was studied by examining the voltage profile of a half-cell during the potassiation/depotassiation process. Bi_2Se_3 and Sb_2Se_3 were also tested under the same conditions for comparison. Fig. 3a–c show the cyclic voltammetry (CV) curves of Bi_2Se_3, $BiSbSe_3$, and Sb_2Se_3 in the initial two cycles with a scan rate of 0.1 mV s^{-1}. For the first cathodic scan, a broad reduction peak appeared at 1.1 V, corresponding to the formation of SEI at the electrode-electrolyte interface during the initial potassiation process (Fig. 3a). The obvious reduction peak at 1.3 V may belong to the conversion reaction from $BiSbSe_3$ to $K_3(Bi,Sb)Se_3$ and (Bi,Sb). The reduction peak at 0.7 V belongs to the conversion reaction of $K_3(Bi,Sb)Se_3$ to form K_2Se and (Bi,Sb), and the alloying reaction: (Bi,Sb)→K(Bi,Sb). The reduction peak at 0.1 V belongs to the alloy reaction: K(Bi,Sb)→K_3(Bi,Sb). In the anodic scan, several oxidation peaks are observed. Two oxidation peaks are located at 0.7 and 1.3 V, which may be attributed to the dealloying reaction: $K_3(Bi,Sb)$→K(Bi,Sb)→(Bi,Sb), respectively. The oxidation peak at 2.2 V may be attributed to the formation of $K_3(Bi,Sb)Se_3$ from the depotassiation of K_2Se and (Bi,Sb). In addition, the CV curve of $BiSbSe_3$ was compared with that of $BiSbSe_3$ with graphite (Fig. S12). Two peaks, at 0.5 V in the discharge process and 0.25 V in the charge process, are observed in the CV curve of $BiSbSe_3$ with graphite, but the CV curve of $BiSbSe_3$ without graphite did not contain these two peaks, indicating two peaks can be attributed to the graphite. Note that the CV curves almost overlap after the 2nd cycle, indicating that the electrochemical reaction is highly reversible. Fig. 3d–f and g–i show the differential capacity (dQ/dV) plots of the first and the second cycles of Bi_2Se_3, $BiSbSe_3$, and Sb_2Se_3. The three clear peaks at 1.3, 0.7, and 0.1V in the dQ/dV plot of $BiSbSe_3$ during the first discharge indicate that there is a three-step reduction process. The peak voltage at 1.3 V is the same as that in Sb_2Se_3, indicating the conversion reaction of $BiSbSe_3$. The peak voltage at 0.7 V is slightly right shifted to the voltage of Bi_2Se_3 and Sb_2Se_3 at 0.6 V, and the peak voltage at 0.1 V is slightly left shifted to the voltage of Bi_2Se_3 and Sb_2Se_3 at 0.2 V, indicating the two-step potassiation reaction of Bi and Sb: (Bi,Sb) → K(Bi,Sb) → K_3(Bi,Sb). The three clear peaks at 0.7, 1.3, and 2.2 V in the dQ/dV plot of $BiSbSe_3$ during the first charge represent the three-step oxidation process. The peak voltage at 0.7 V is slightly right shifted to the voltage of Bi_2Se_3 and Sb_2Se_3 at

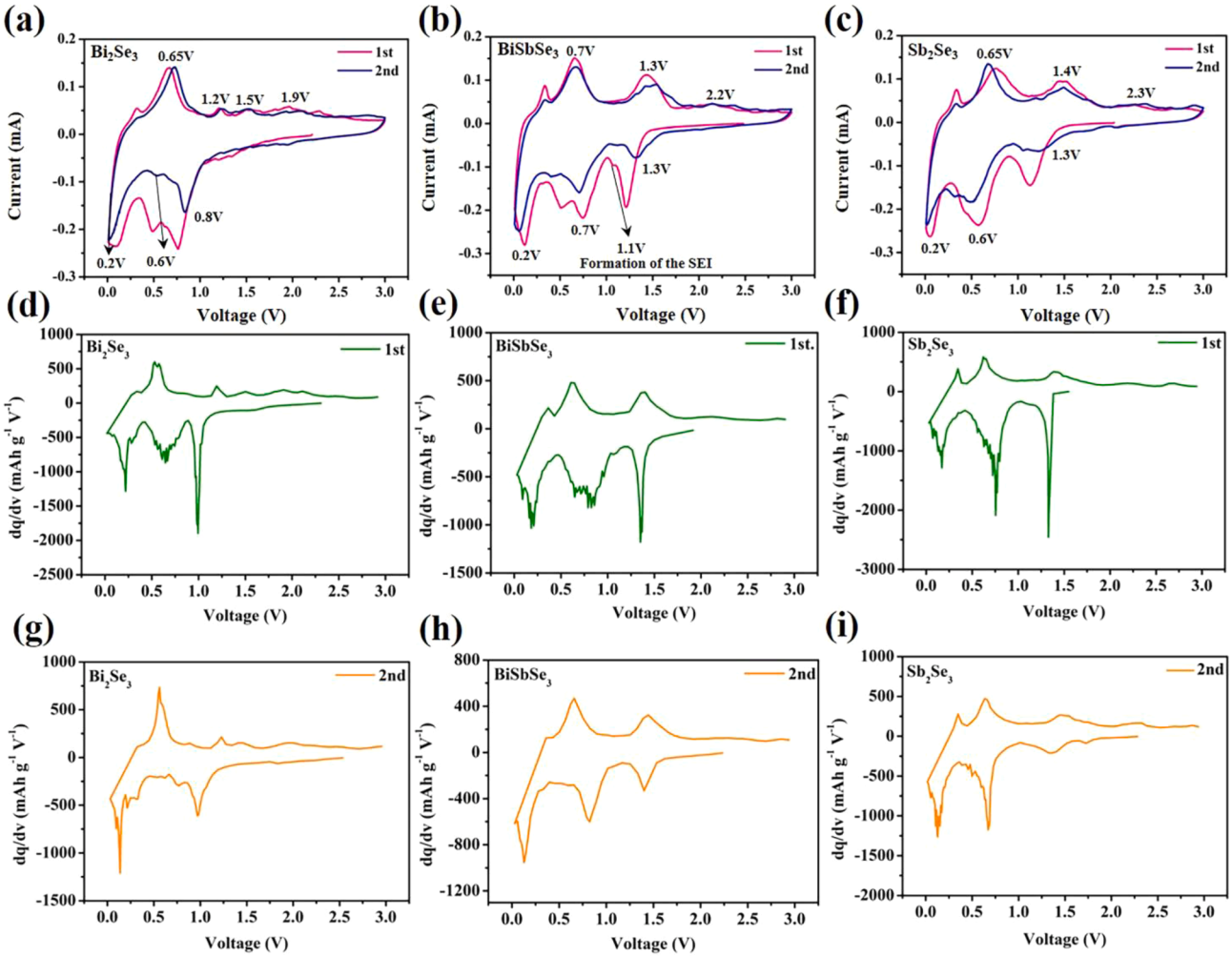

Fig. 3. (a–c) CV curves, and differential capacity plots obtained for the (d–f) first and (g–i) second cycles of the Bi_2Se_3, $BiSbSe_3$, and Sb_2Se_3 electrodes.

0.65 V, and the peak voltage at 1.3 V is slightly left shifted to Bi_2Se_3 at 1.5 V and the peak voltage of Sb_2Se_3 at 1.4 V. This indicates the two-step depotassiation reaction of Bi and Sb: $K_3(Bi,Sb) \rightarrow K(Bi,Sb) \rightarrow (Bi,Sb)$. The peak voltage at 2.2 V is slightly left shifted to the voltage of Sb_2Se_3 at 2.3 V, which is characteristic of the depotassiation of K_2Se and (Bi,Sb) to form $K_3(Bi,Sb)Se_3$. In the second cycle, similar potassiation and depotassiation reactions were observed. The CV curve and dQ/dV plots of $Bi_{1.75}Sb_{0.25}Se_3$ and $Bi_{0.25}Sb_{1.75}Se_3$ were also investigated (Fig. S13). The results of $Bi_{1.75}Sb_{0.25}Se_3$ and $Bi_{0.25}Sb_{1.75}Se_3$ were consistent with those of Bi_2Se_3 and Sb_2Se_3, respectively [35,38,39].

In order to explore the influence of different Bi and Sb ratios on electrochemical performance in the $Bi_{2-x}Sb_xSe_3$ system, the cycle performance and rate capability of $Bi_{2-x}Sb_xSe_3$ (x = 0, 0.25, 1, 1.75, 2) electrodes were investigated. Fig. 4a shows the cycle performance of $Bi_{2-x}Sb_xSe_3$ (x = 0, 0.25, 1, 1.75, 2) at a current density of 100 mA g^{-1}. The decay of the specific capacity observed in five samples before the first 10 cycles may be due to the generation of SEI and partial dissolution of the active material. The discharge and charging specific capacities of $BiSbSe_3$ are 428 mA h g^{-1} and 423 mA h g^{-1} after 100 cycles, respectively, which is significantly higher than those of the other four materials. These results indicate $BiSbSe_3$ with high capacity and cycle stability for PIBs. Figs. 4b and S14 show the rate performance and the corresponding charge/discharge curves of the $Bi_{2-x}Sb_xSe_3$ (x = 0, 0.25, 1, 1.75, 2) electrodes from 0.1 to 10 A g^{-1}. Obviously, the $BiSbSe_3$ electrode shows a higher discharge capacity than that of $Bi_{2-x}Sb_xSe_3$ (x = 0, 0.25, 1.75, 2) at high current density (1−10 A g^{-1}). When the current densities are 0.1, 0.2, 0.5, 1.0, 2.0, 4.0, 8.0, and 10 A g^{-1}, the discharge capacity of the $BiSbSe_3$ electrode delivers average discharge

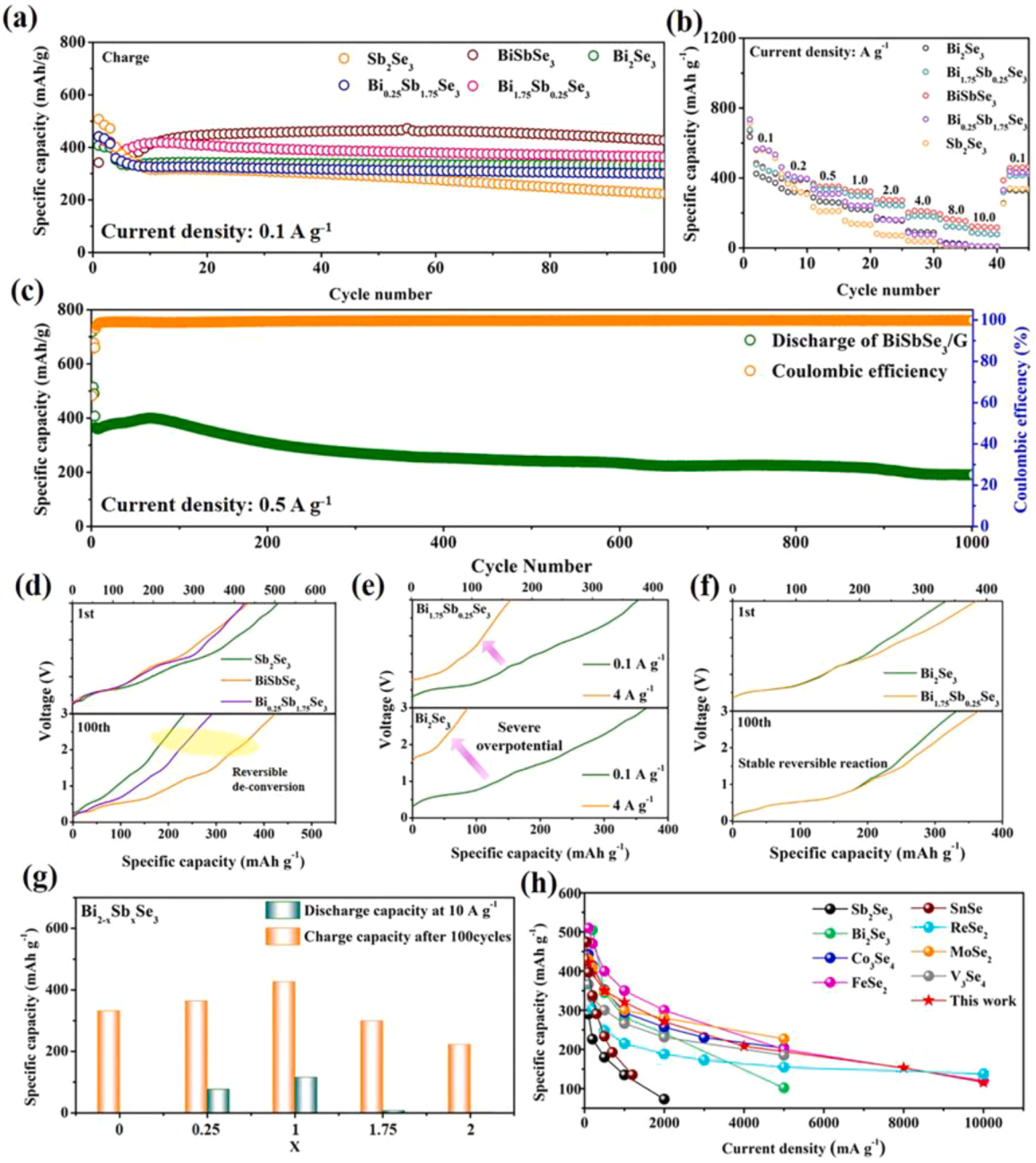

Fig. 4. (a) Cycling performance of the $Bi_{2-x}Sb_xSe_3$ electrodes at 0.1 A g^{-1}. (b) Rate capabilities of the $Bi_{2-x}Sb_xSe_3$ electrodes at various current densities. (c) Long-term cycling performance of the $BiSbSe_3$ electrode at 0.5 A g^{-1}. Voltage profiles of (d) $BiSbSe_3$, $Bi_{0.25}Sb_{1.75}Se_3$ and Sb_2Se_3 electrodes at 0.1 A g^{-1} for the 1st and 100th cycles, (e) Bi_2Se_3 and $Bi_{1.75}Sb_{0.25}Se_3$ electrodes at 0.1 and 4 A g^{-1}, and (f) Bi_2Se_3 and $Bi_{1.75}Sb_{0.25}Se_3$ electrodes at 0.1 A g^{-1} for the 1st and 100th cycles. (g) Discharge capacity and charge capacity of $Bi_{2-x}Sb_xSe_3$ electrodes. (h) Rate performance comparison of $BiSbSe_3$ with previously reported anode materials.

capacities of 422, 393, 350, 321, 271, 208, 153, and 116 mA h g^{-1}, respectively. When the current density returns to 0.1 A g^{-1}, the specific capacity of the $BiSbSe_3$ electrode quickly returns to 458 mA h g^{-1}, and remains stable for further cycling. The cycle performance of $BiSbSe_3$ at a current density of 500 mA g^{-1} is shown in Fig. 4c. After 1,000 cycles, the discharge specific capacity of $BiSbSe_3$ still retains 191.3 mA h g^{-1}, and the Coulombic efficiency reaches 99.8%, indicating high stability and high reversibility. All the calculation of the battery capacity was based on the total mass of $Bi_{2-x}Sb_xSe_3$ and graphite. Additionally, the cycle performance of the raw material ($BiSbSe_3$ without graphite) and the morphology of the raw and modified materials ($BiSbSe_3$ with graphite) after 50 cycles are shown in Figs. S15 and 16. Fig. S17 shows the photographs, SEM images and TEM images of the Bi_2Se_3, $BiSbSe_3$ and Sb_2Se_3 electrodes after 50 cycles at 0.5 A g^{-1}. First, it can be observed that the Sb_2Se_3 electrode is more severe cracking than the Bi_2Se_3 and $BiSbSe_3$ electrode (Fig. S17a−f). These result are the same as the TEM images (Fig. S17g−i). The collapse of Sb_2Se_3 nanostructures after continuous charge/discharge cycling caused crack on electrode surface because of fuzzy fragments (Fig. S17g). In contrast, Fig. S17h and i showed nanoparticles encapsulated in flake graphite uniformly, so that the disassembled $BiSbSe_3$ and Bi_2Se_3 electrodes after 50 cycles maintain a complete electrode surface. The reason could be contributed to that the bond length of Bi-Se is longer than Sb-Se where the lattice softening effect is attributed to the low bond energy (or the long bond length) [33]. The Bi-Se bond is softer than Sb-Se and can alleviate fragmentation caused by volume expansion. In addition, with inducing Sb into the Bi_2Se_3 lattice, the rhombohedral Bi_2Se_3 structure would transform to the orthorhombic phase [34]. The composition-induced structural phase transition largely altered the electronic properties, the accompanying bond breaking and elongation effectively soften the chemical bonding occur. These results could explain why there were almost no cracks on the surface of $BiSbSe_3$ electrode (Fig. S17e), but there were some cracks on the surface of the Bi_2Se_3 electrode. The result of Fig. S17 can correspond to the result of Fig. 4a. After inducing the Bi atoms into the Sb_2Se_3 lattice, the cycling and rate performance of $BiSbSe_3$ ternary phase is better than that of the Bi_2Se_3 and Sb_2Se_3 binary phase. In order to observe the influence of Bi replacing Sb in the Sb_2Se_3 phase, charging curves of Sb_2Se_3, $BiSbSe_3$, and $Bi_{0.25}Sb_{1.75}Se_3$ at the 1st and 100th cycles are shown in Fig. 4d. The potential plateaus of the three samples are very obvious during the first cycle. However, the capacity of Sb_2Se_3 decreased by about 55% after 100 cycles, and its electrochemical plateaus became insignificant, indicating that the structure of Sb_2Se_3 is very unstable during the potassiation/depotassiation process. It is noteworthy that the electrochemical plateaus of $BiSbSe_3$ and $Bi_{0.25}Sb_{1.75}Se_3$ are still obvious after 100 cycles, indicating electrochemical stability improvement when Bi replaces Sb. In addition, the influence of Sb substituted by Bi in the Bi_2Se_3 phase was also investigated. Fig. 4e shows that the overpotential of $Bi_{1.75}Sb_{0.25}Se_3$ is lower than that of Bi_2Se_3 at a high current density of 4 A g^{-1}. This is due to the addition of Sb and the synergistic effect of Bi and Sb enhancing the spontaneous adsorption of K with the promotion of high rate capability [40].

Fig. 4f shows a comparison of the Bi_2Se_3 and $Bi_{1.75}Sb_{0.25}Se_3$ QV curves at 0.1 A g^{-1} after 1 and 100 cycles; there are no overpotential and potential plateaus remaining after 100 cycles. This means that $Bi_{2-x}Sb_xSe_3$ has better stability and reversibility when the content of Bi is relatively high. The discharge capacity at 10 A g^{-1} and the charge capacity at 0.1 A g^{-1} after 100 cycles of $Bi_{2-x}Sb_xSe_3$ (x = 0, 0.25, 1, 1.75, 2) are compared in Fig. 4g. The capacities of Sb_2Se_3 and $Bi_{0.25}Sb_{1.75}Se_3$ before 3 cycles are higher than that of $Bi_{2-x}Sb_xSe_3$ (x = 0, 0.25, 1) (Fig. 4a). After three cycles or high rates, the capacity of $Bi_{2-x}Sb_xSe_3$ (x = 0, 0.25, 1) gradually remains stable. In contrast, the capacities of Sb_2Se_3 and $Bi_{0.25}Sb_{1.75}Se_3$ rapidly decay because they undergo huge volume expansion that results in severe pulverization of the active materials. In short, the cycle and rate performance tests show that when either Sb_2Se_3 or Bi_2Se_3 is substituted by Bi or Sb, the cycle stability and rate capability are better than those of the original Sb_2Se_3 or Bi_2Se_3 [41].

Fig. 4h shows a comparison of the current density and specific capacity of $BiSbSe_3$ with those of other reported selenium-based anodes. The rate performance of most selenium-based anodes is limited to about 5 A g^{-1}, except for $BiSbSe_3$, $FeSe_2$ and $ReSe_2$. Although the discharge capacity of $BiSbSe_3$ is not the highest due to its theoretical specific capacity, it is still higher than that of most selenium-based material anodes. In addition, the discharge capacity of $BiSbSe_3$ is lower than that of $ReSe_2$ because of the synthesis of NG/$ReSe_2$/MXene heterostructure. Therefore, $BiSbSe_3$ can also deliver 116 mA h g^{-1} at a higher current density of 10 A g^{-1}, indicating that $BiSbSe_3$ electrodes have certain advantages at high current densities [14,35,42-47].

The related charge storage mechanism and kinetics process were analyzed to further study the potassium storage performance of $BiSbSe_3$. Fig. 5a shows analysis of the capacitive effect of $BiSbSe_3$ based on CV curves at various scan rates (0.2–1.0 mV s^{-1}). As expected, the scan rate increases with similar shapes, indicating that the $BiSbSe_3$ electrode has fast kinetic. According to the power law relationship, the relationship between peak current (i) and scan rate (v) can be described as $i = av^b$, where a and b are constants. The "b" value represents the degree of capacitive effect: b value of 0.5 represents an extreme diffusion control process and an extreme capacitive control process is represented by b value of 1.0. By plotting log(i) and log(v), the b value can be extracted from the slope of the linear relationship. The b-values of peaks one through six are 0.60, 0.90, 0.61, 0.81, 0.94, and 0.98 (Fig. 5b), exhibiting battery and capacitance contributions. The capacitance contribution can be further quantified using the following equation.

$$i(v) = k_1 v + k_2 v^{1/2} \quad (1)$$

where k_1 and k_2 are constant values corresponding to capacitive control and diffusion control processes, respectively. As presented in Fig. 5c, the capacitance ratio in the total storage process is 67% at 0.4 mV s^{-1}. Fig. 5d shows the contribution of pseudocapacitance behavior at different scan rates. At scan rates of 0.4, 0.6, 0.8, and 1 mV s^{-1}, the capacitance ratios are 58%, 67%, 71%, 74%, and 76%, respectively. At a lower scan rate of 0.2 mV s^{-1}, the capacitance contribution still reaches 58%. These results demonstrate that the pseudocapacitor storage occupies a relatively high proportion of the total capacity. Fig. S18 shows a comparison of the capacitive contribution of $Bi_{2-x}Sb_xSe_3$ (x = 0 and 0.25). The results are consistent with those of the electrochemical performance. Figs. S19 and 20 show the CV curves of Sb_2Se_3 and $Bi_{0.25}Sb_{1.75}Se_3$ at various scan rates, yet b value cannot be calculated due to disappearance of the potential plateaus. Next, the galvanostatic intermittent titration technique (GITT) was then used to evaluate the diffusion coefficient of K^+ in the $BiSbSe_3$ electrode by applying a series of pulse currents under 0.1 A g^{-1} for 0.33 h with rest intervals of 0.67 h (Fig. S21). Before the GITT measurement, the assembled battery was discharged/charged at 0.05 mA g^{-1} for three cycles. According to Fick's second law, D_{K+} can be calculated by the following equation [48].

$$D_{K^+} = \frac{4}{\pi\tau}\left(\frac{m_B V_M}{M_B S}\right)^2 \left(\frac{\Delta E_S}{\Delta E_\tau}\right)^2 \tau \ll \frac{L^2}{D} \quad (2)$$

where m_B, M_B and V_M are the mass, molar mass and molar volume of the electrode material, respectively, τ is the relaxation time, S is the interfacial area of the electrode, ΔE_t and ΔE_s are the voltage changes during the constant current phase after each balance process, and L is the thickness of the electrode. Fig. S22 shows the cross-section of the electrode. The D_{K+} value of $BiSbSe_3$ ranges from 4.68×10^{-12} to 3.036×10^{-11} at the potassiation voltage and from 1.23×10^{-11} to 2.54×10^{-10} at the depotassiation voltage (Fig. 5e). This result indicates that $BiSbSe_3$ exhibits rapid K^+ diffusion due to the solid solution structure. In addition, the electrochemical conversion reaction of $BiSbSe_3$ during potassiation and depotassiation was explored by *in-situ* electrochemical impedance spectroscopy (EIS), as shown in Fig. 5f. Generally, all Nyquist diagrams are composed of a semicircle in the high/mid-frequency region and a line in the low-frequency region. In the initial cycle, the resistance

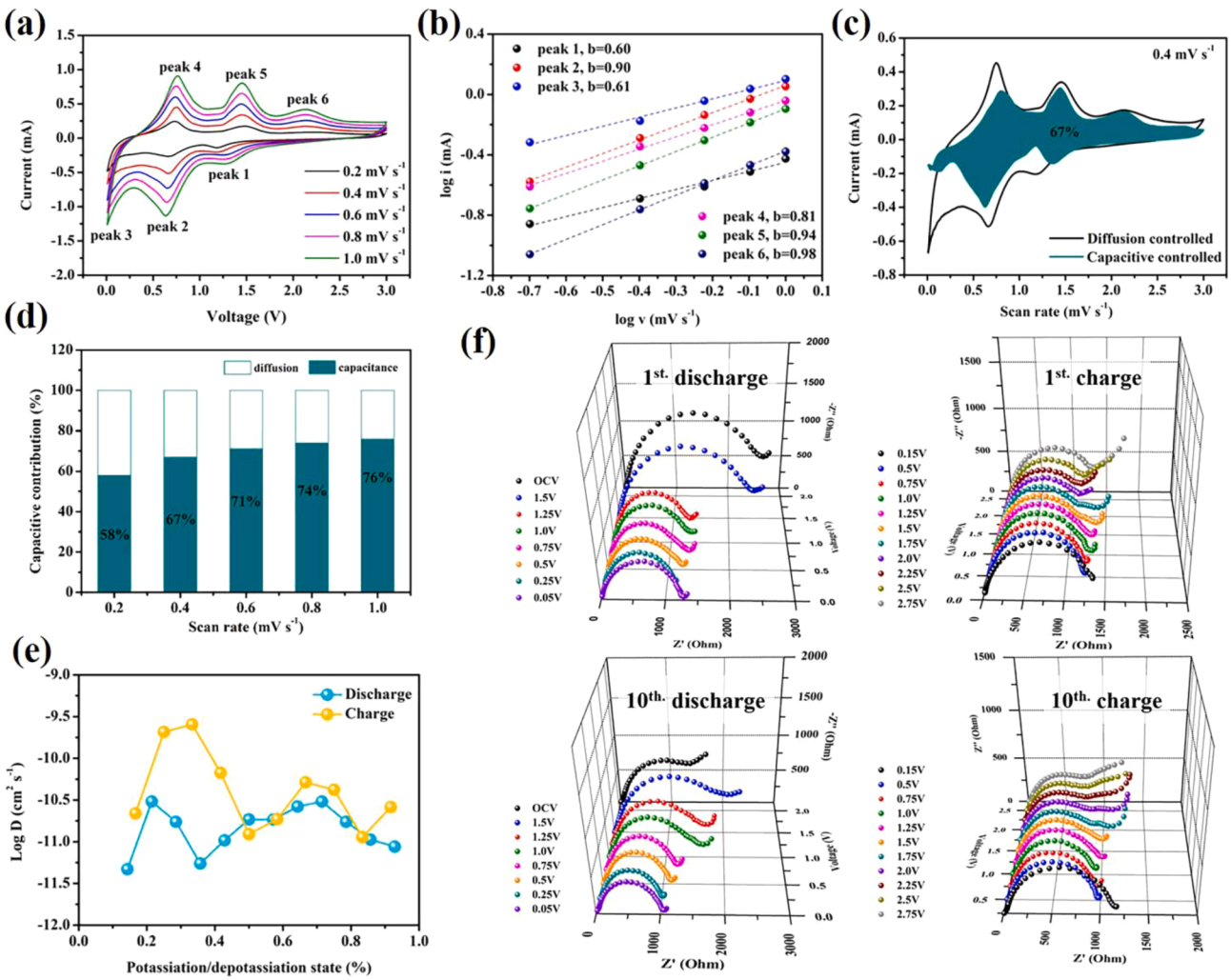

Fig. 5. (a) CV curves at various scan rates in the range of 0.2–1.0 mV s^{-1}. (b) Linear relation of log(i, peak current) and log(v, scan rate). (c) Pseudocapacitive contribution at the scan rate of 0.4 mV s^{-1}. (d) Contribution ratio of the capacitive and diffusion-controlled capacities of $BiSbSe_3$ at different scan rates. (e) GITT analysis of $BiSbSe_3$ at 0.1 A g^{-1}. (f) *In-situ* EIS test performed at selected potentials. *In-situ* EIS measurements of the $BiSbSe_3$ electrode for the 1st and 10th cycles at pre-selected potentials.

slightly increases due to the insertion of an initial K^+. As confirmed with the CV curve, a broad reduction peak appears at 1.3 V, which corresponds to irreversible insertion because of the formation of a SEI and the conversion reaction of forming $K_3(Bi,Sb)Se_3$ and (Bi,Sb). The resistance decreased significantly after 1.25 V, which was attributed to the alloy reaction of (Bi,Sb). When gradually charging to 0.75 V, the alloying reaction of $K_3(Bi,Sb)$ leads to a decrease in resistance. The Nyquist plot of the $BiSbSe_3$ electrode in the 10th cycle was introduced to study the structural evolution with electrochemical kinetics after stabilization of the $BiSbSe_3$ electrode. During potassiation and depotassiation processes, $BiSbSe_3$ showed similar trends before and after 10 cycles. It is worth noting that the $BiSbSe_3$ electrode exhibits very low resistance even after 10 cycles. These results prove the excellent kinetics of $BiSbSe_3$.

We carried out DFT calculations using the Vienna Ab initio Simulation Package (VASP) to theoretically explore the process of inserting K^+ into $BiSbSe_3$ (Figs. 6a and S23). The calculated equilibrium lattice parameters of $BiSbSe_3$ after inserting the potassium ions K1 to K8 are shown in Table S1. There are only a few symmetry sites suitable for insertion of potassium ions because of the large radius of K^+ (1.38 Å) [49]. At the same time, the intercalation energy (Ei) of potassium ions is calculated by the following formula equation:

$$E_i = (E_{total} - E_{sub} - nE_K)/n \quad (3)$$

where E_{total} is the total energy of the K inserted systems, E_{sub} and E_K are the energies of the substrate and the K atom in bulk, respectively, and n is the number of K^+ ions inserted into the lattice [50]. The Ei for the intercalation of the first K^+ into the $BiSbSe_3$ lattice is −0.53 eV, which means that the reaction is exothermic and the interaction is attractive, indicating a favorable reaction [51]. Interestingly, the insertion of the second K^+ is even more advantageous, the Ei (−1.22 eV) is more negative than for the insertion of the first (−0.53 eV), but will cause more serious lattice distortion. The lattice parameter a is moderately increased by 6.17%, b is moderately decreased by 11.77%, and c is increased significantly by 33.33%, resulting in a 16.47% volume expansion and Sb-Se bond breakage (shown by arrows in Fig. 6a). Likewise, the Bi-Se and Sb-Se bonds are gradually elongated. With additional K^+ insertions, more original Sb-Se bonds are broken. When the eighth K^+ is embedded in the $BiSbSe_3$ lattice, the lattice parameters a and b are moderately increased by 6.17% and 11.68%, respectively, while c is greatly increased by 37.48%, resulting in volume expansion (about 60%) and fracture of Bi-Se bonds (indicated by arrows in Fig. 6a). If more K^+ are added, more Sb-Se and Bi-Se bonds will be destroyed, and the calculation cannot converge, indicating collapse of the crystal lattice, which is consistent with the result of the operando XRD [32,52]. After K^+ is inserted into the orthorhombic crystal of $BiSbSe_3$, the cubic crystal $K_3(Bi,Sb)Se_3$ originates. It is worth noting that it is feasible to

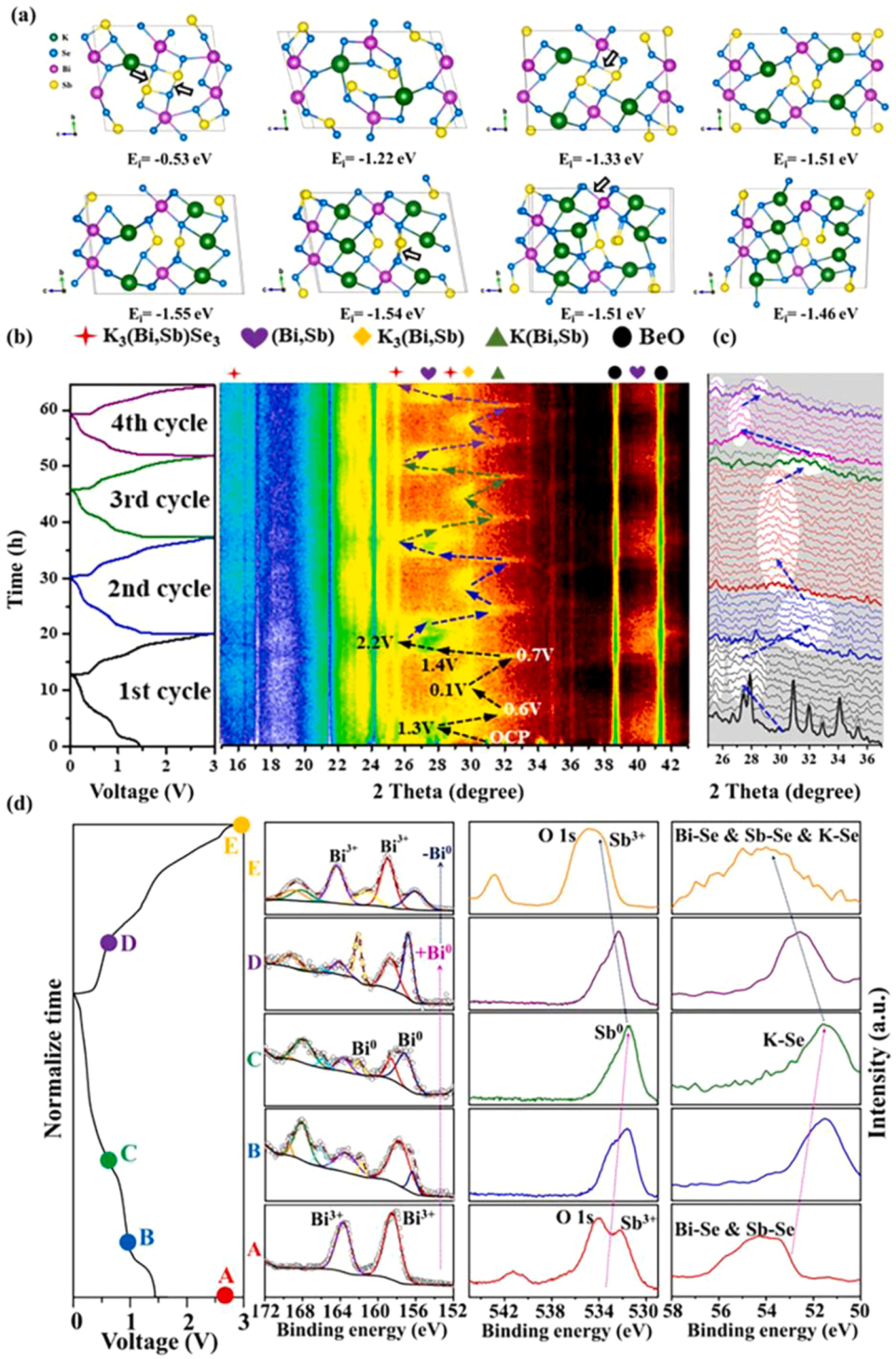

Fig. 6. (a) Unit cell structure of $BiSbSe_3$ with 1–8 K atom after geometry optimization. (b) *In situ* contour plot of the operando XRD result of the $BiSbSe_3$ electrode during the K-ion insertion/extraction process of the initial four cycles and (c) corresponding line plots at first cycle. (d) *Ex-situ* XPS spectra of Bi 4f, Sb 3d and Se 3d during the discharging/charging process.

convert $BiSbSe_3$ into $K_3(Bi,Sb)Se_3$ through the DFT calculation. From Table S2, the substitution of Bi or Sb will not cause collapse or expansion of the $K_3(Bi,Sb)Se_3$ crystal lattice. The calculated volume of $K_3(Bi,Sb)Se_3$ is between K_3BiSe_3 and K_3SbSe_3, speculating that $BiSbSe_3$ will not be converted into K_3BiSe_3 and K_3SbSe_3, but rather into $K_3(Bi,Sb)Se_3$ (Fig. S24). Fig. 6b and c show a two-dimensional view of the *in-situ* XRD pattern of $BiSbSe_3$ for the initial four cycles along with their corresponding charge/discharge curves and corresponding line plots at first cycle. The waterfall diagram of the in situ XRD patterns of the $BiSbSe_3$ electrode at the first cycle was shown in Fig. S25. With the insertion of K^+, the intensity of the $BiSbSe_3$ phase peaks gradually decreased. When discharging from the open circuit voltage (OCV) to 1.3 V, several new peaks are observed at 16°, 25.7°, 27.5°, and 28.6°. Among these new peaks, that at 27.5°corresponds to the (0 1 2) facets of the (Bi,Sb) phase (PDF no. 01-081-3946). The peaks at 16°, 25.7°, and 28.6° may correspond to the (1 1 1), (2 2 0), and (3 1 0) facets of $K_3(Bi,Sb)Se_3$. At the same time, the peak at 25.7° gradually weakened, but the intensity of the peaks at 28° and 40° did not weaken, indicating the second step of

the conversion reaction ($K_3(Bi,Sb)Se_3$ converted to (Bi,Sb) and K_2Se). The simulated XRD results are consistent with the *in-situ* XRD experimental data (Fig. S26). However, poor crystallinity or small particle size caused an unclear K_2Se signal. Therefore, the formation of K_2Se is confirmed by the *ex-situ* XRD, and Fig. S27 shows that the intensity of the peak at 20° gradually increases when the discharge process reaches 0.01 V, which can be attributed to the formation of K_2Se (PDF no. 00-023-0470). When discharging to 0.6 V, a peak at 0.6 V is attributed to the formation of K(Bi,Sb) (PDF 04-010-8776), indicating the alloy reaction of (Bi,Sb). As the reaction proceeded, more K^+ ions react with the K(Bi,Sb) alloy to form $K_3(Bi,Sb)$ and a peak appears at 0.1 V, corresponding to (2 2 0) facets of the $K_3(Bi,Sb)$ phase (PDF No. 00-019-0935). The peak of $K_3(Bi,Sb)$ gradually disappears when charging to 0.7 V, suggesting the dealloying reaction by reappeared K(Bi,Sb). In addition, with continuous charging to 1.4 and 2.2 V, the $K_3(Bi,Sb)$ peaks completely disappeared, which is coupled with the reappearance of (Bi, Sb) and then $K_3(Bi,Sb)Se_3$. One can be observed that there are no peaks related to $BiSbSe_3$, indicating that the conversion reaction in the first step is irreversible. The second conversion reaction and alloying reaction in the subsequent discharge process, as well as the dealloying and conversion reactions in the charging process, are all reversible. The results of the *in-situ* XRD shown in the 2nd–4th circles can be verified as reversible after the 2nd cycle. This whole phase evolution is consistent with the CV results.

To further determine the potassiation/depotassiation process of $BiSbSe_3$, a series of XPS spectra of Bi 4f, Sb 3d and Se 3d is shown in Fig. 6b. First, in the Bi 4f spectrum corresponding to points A to C, the $Bi^0_{7/2}$ and $Bi^0_{5/2}$ peaks are gradually enhanced at 157 and 162 eV. Then, the $Bi^0_{7/2}$ and $Bi^0_{5/2}$ peaks are gradually weakened from point D to E. The Bi 4f spectrum can be split into three peaks for SEI formation, located at 169.4, 168.2, and 166.2 eV, which are assigned to the NSO_2^- (orange line), SO_2F^-(green line), and SO_3^-(light blue line), respectively [53]. At the same time, the $Sb^{3+}_{5/2}$ peak (531.5 eV) shifts to lower binding energy to form $Sb^0_{5/2}$ (530.5 eV) [54]. The results show two transformations between Bi^{3+} and metallic Bi^0, and between Sb^{3+} and metallic Sb^0. This also explains the plateau of the alloying process. When charging to 3 V, the Sb^{3+} peak gradually increased, while the Sb^0 peak shifted to a higher binding energy to form Sb^{3+}, indicating the formation of $K_3(Bi,Sb)Se_3$. In addition, the Se 3d spectrum of the $BiSbSe_3$ electrode before discharge/charge process is centered at 54.3 eV, and can be deconvoluted into the following two distinct peaks: Bi-Se and Sb-Se. When discharging to the first (point B) and second (point C) plateaus, the main peak gradually shifts to lower binding energies, which is likely due to the formation of K_2Se resulting in the electron-donor effect of K^+ [55]. When charging to 3.0 V, the Se 3d spectrum corresponding to point D to point E indicates that the main peak gradually returns to close to its original position. The reason for the slight shift is that the deconvolution is Bi-Se, Sb-Se and K-Se instead of the original Bi-Se and Sb-Se. This result is highly consistent with the XRD analysis results.

Fig. 7 shows *ex-situ* TEM results of the $BiSbSe_3$ electrode at different potentials in the first cycle to study the microstructure and products of the K^+ insertion/extraction in $BiSbSe_3$. The low-resolution TEM images show that the $BiSbSe_3$ morphology changes from bulk material to nanoparticle aggregates during the charging/discharging process (Fig. 7a). After discharging to 0.5 V, the HRTEM image contains several nanocrystal areas with crystal lattices of 0.231, 0.287 and 0.336 nm, which are attributed to the (3 1 1) plane of the K_2Se phase and the (3 1 1) and (2 2 0) planes of the K(Bi,Sb) phase, respectively (Fig. 7b). The corresponding SAED patterns can be assigned to the (1 1 1) plane of the K_2Se phase and the (4 0 0) and (3 1 1) planes of the K(Bi,Sb) phase (Fig. 7c). After discharging to 0.01 V, $BiSbSe_3$ can still be maintained the same structure as when discharging to 0.5 V, as shown in Fig. 7d. And, lattice fringes of 0.319, 0.317, and 0.231 nm can be observed in the HRTEM image and are attributed to the (3 1 1) plane of the K_2Se phase

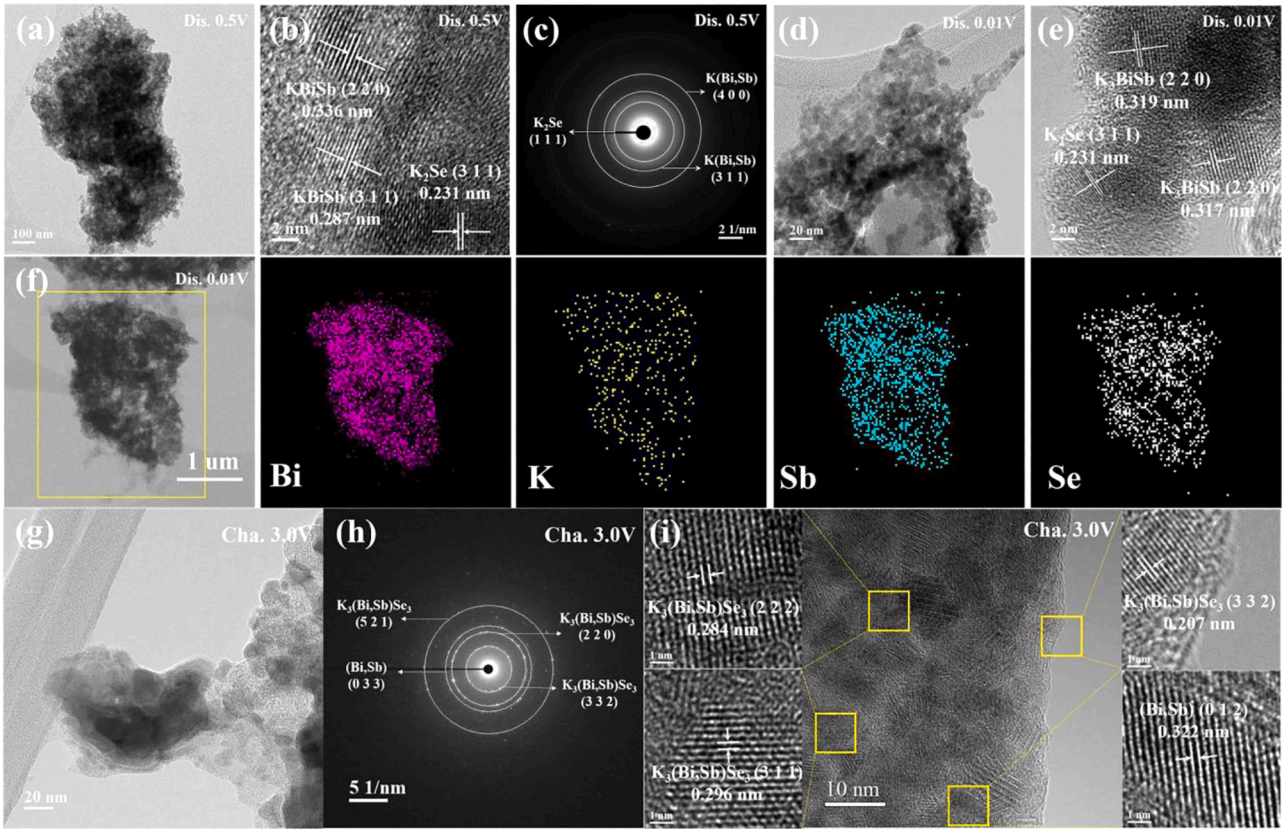

Fig. 7. (a) TEM, (b) HRTEM and (c) SAED images of $BiSbSe_3$ after discharging to 0.5 V. (d) TEM, (e) HRTEM, and (f) EDS mapping images of $BiSbSe_3$ after discharging to 0.01 V. (g) TEM, (h) SAED, and (i) HRTEM images of $BiSbSe_3$ after charging to 3.0 V.

and the (2 2 0) plane of the K_3(Bi,Sb) phase (Fig. 7e). The element mapping of the completely discharged electrode is shown in the Fig. 7f and indicates uniform distribution of the K, Bi, Sb and Se elements. During the discharging process, the lattice fringes in the HRTEM image and electron diffraction rings in the SAED pattern indicate the formation of a mixture of K_x(Bi,Sb) alloys, including K(Bi,Sb) and K_3(Bi,Sb). This confirms the alloying reaction mechanism of the $BiSbSe_3$ electrode, which is consistent with the *in-situ* XRD results. At a fully charged state of 3.0 V, K_3(Bi,Sb)Se_3 diffraction peaks can be clearly observed, which indicate that the fully charged products are K_3(Bi,Sb)Se_3 and (Bi,Sb). Additionally, it can be observed that the structure of nanoparticle aggregate can still be maintained even at the full K-ion insertion state, highlighting the superiority of the composite (Fig. 7g). Fig. 7h shows that the corresponding SAED pattern can be indexed into the (0 3 3) planes of the (Bi,Sb) phase, and the (5 2 1), (2 2 0), and (3 3 2) planes of the K_3(Bi,Sb)Se_3 phase, which are in agreement with the HRTEM (Fig. 7i) and *in-situ* XRD results. Therefore, these results support the potassiation intermediate and depotassiation products constituted by a mixture of phases of K_3(Bi,Sb)Se_3 and (Bi,Sb).

According to the above *in-situ* and *ex-situ* results, a reaction mechanism shown by the schematic diagram in Fig. 8 is inferred. During the discharging process, $BiSbSe_3$ undergoes the following irreversible reaction: $BiSbSe_3 + 3K^+ + 3e^- \rightarrow K_3(Bi,Sb)Se_3 + (Bi,Sb)$. Then, K_3(Bi,Sb)Se_3 undergoes reversible conversion reaction that results in (Bi,Sb) and K_2Se. Next, (Bi,Sb) can react with K to form K(Bi,Sb), which in turn can further react with K to form K_3(Bi,Sb) (alloying reaction). During the charging process, K_3(Bi,Sb) undergoes the following dealloying reaction: $K_3(Bi,Sb) \rightarrow K(Bi,Sb) \rightarrow (Bi,Sb)$. Then, (Bi,Sb) and K_2Se are oxidized to K_3(Bi,Sb)Se_3 by conversion reaction. Importantly, the reason why K_3(Bi,Sb)Se_3 is significant intermediate phase during cycling is that the formation of K_3(Bi,Sb)Se_3 is accompanied by that of BiSb alloys. Therefore, the following potassium-ion storage mechanism of $BiSbSe_3$ is proposed, including conversion reaction and alloying process, as follows:

Irreversible conversion reaction:

$$BiSbSe_3 + 3K^+ + 3e^- \rightarrow K_3(Bi,Sb)Se_3 + (Bi,Sb) \quad \text{(I)}$$

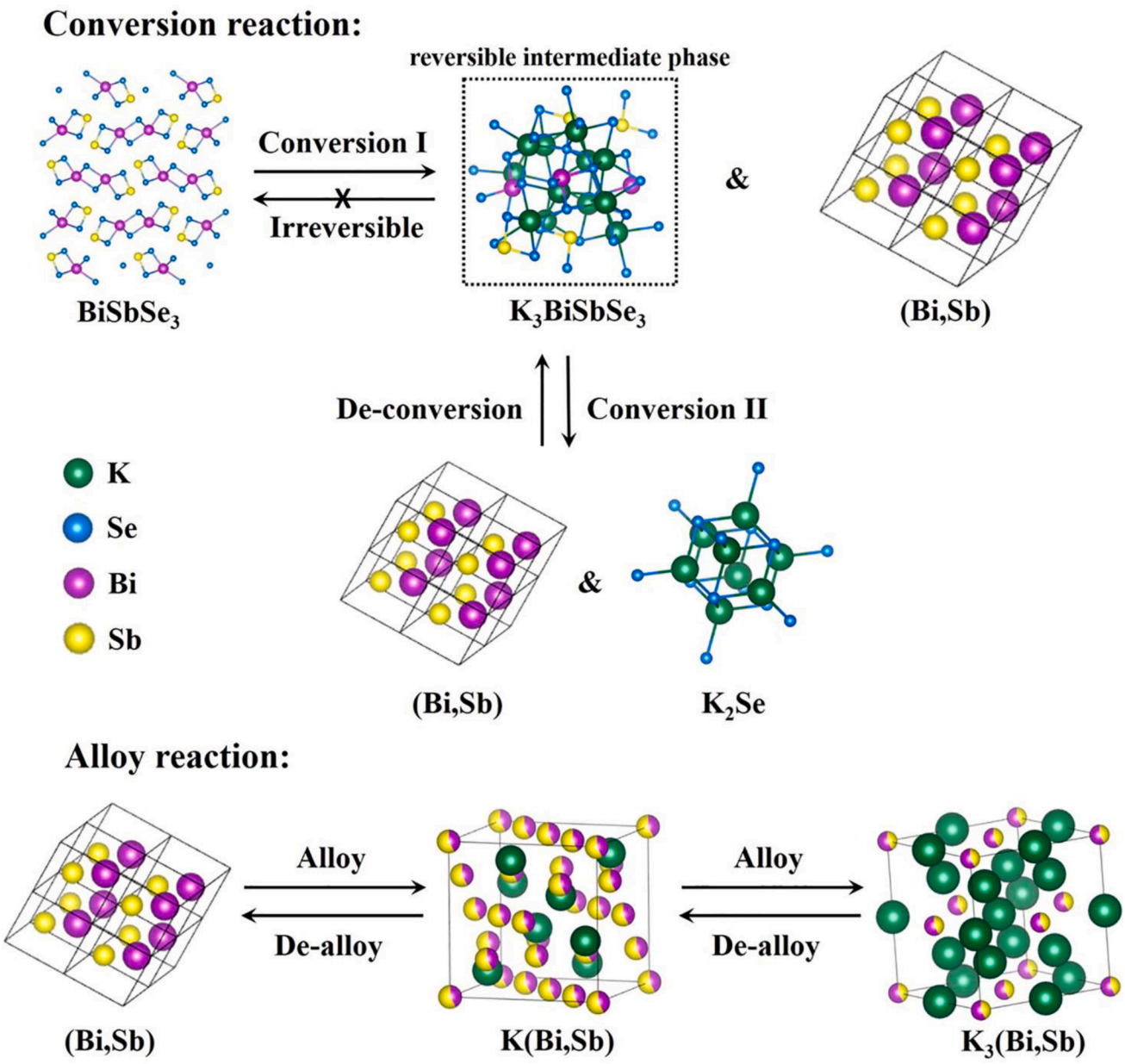

Fig. 8. Schematic illustration of the K^+ storage mechanism of $BiSbSe_3$ during the alloying and conversion process.

Reversible conversion reaction:

$$K_3(Bi,Sb)Se_3 + 3K^+ + 3e^- \leftrightarrow (Bi,Sb) + 3K_2Se \quad \text{(II)}$$

Reversible alloying/dealloying reactions:

$$2(Bi,Sb) + 2K^+ + 2e^- \leftrightarrow 2K(Bi,Sb) \quad \text{(III)}$$

$$2K(Bi,Sb) + 4K^+ + 4e^- \leftrightarrow 2K_3(Bi,Sb) \quad \text{(IV)}$$

Ternary solid solutions can be formed by substituting atoms of comparable size and charge, such as bismuth and antimony ($BiSbS_3$), or chalcogen substitutions, such as sulfur, selenium or tellurium (SnSSe). In this work, Bi_2Se_3 and Sb_2Se_3 are used as models to form a ternary alloy solid solution ($Bi_{2-x}Sb_xSe_3$) through substitution of bismuth/antimony. Interestingly, $Bi_{2-x}Sb_xSe_3$ inherits properties that cannot be achieved by the simple size adjustment of its parent binary analog. From the XRD analysis, the $Bi_{2-x}Sb_xSe_3$ phase has the orthorhombic crystal structure of Bi-doped Sb_2Se_3 when x increases to/exceeds 1. Furthermore, in the lower Sb content range of x = 0–0.25, $Bi_{2-x}Sb_xSe_3$ maintains the rhombohedral crystal structure of Sb-doped Bi_2Se_3. More importantly, the structural changes during the phase transition induce significant changes in the electronic band structure and lattice dynamics, thereby providing a basis for tuning the electrochemical properties of $Bi_{2-x}Sb_xSe_3$. The structural change of $Bi_{2-x}Sb_xSe_3$, from the rhombohedral (Bi_2Se_3-based) and orthorhombic (Sb_2Se_3-based) phases via Bi-Sb alloying, is accompanied by a significant chemical bond softening, which enhances fracture toughness to withstand the large volume changes of potassiation/depotassiation, thereby improving electrochemical performance. After 100 cycles, the electrochemical plateau of Sb_2Se_3 becomes indistinct, indicating that the structure of Sb_2Se_3 is very unstable during the potassiation/depotassiation process. However, the electrochemical plateaus of the orthorhombic crystals of $BiSbSe_3$ and $Bi_{1.75}Sb_{0.25}Se_3$ are still evident after 100 cycles, indicating that the addition of Bi contributes to the electrochemical stability. Additionally, the charge/discharge curves corresponding to the rate performance indicate that the addition of Sb can reduce the overpotential, resulting in high rate capability. In conclusion, when Sb_2Se_3 or Bi_2Se_3 is substituted by Bi or Sb, the electrochemical stability and rate performance are better than those of pristine Sb_2Se_3 or Bi_2Se_3, which can be attributed to the synergistic effect of band structure modification and chemical bond softening. The mechanism of $BiSbSe_3$ was also analyzed using *in-situ* XRD during the potassiation/depotassiation process. After discharging, $BiSbSe_3$ was first converted into a reversible intermediate phase of $K_3(Bi,Sb)Se_3$ and metals (Bi,Sb). It is worth noting that metastable intermediate compounds usually have higher free energies and can easily initiate new reactions that break down unstable old bonds into stable bonds. Qi et al. reported that the metastable phase of $FeCN_2$ causes lower intercalation and conversion reaction energies during the discharge/charge process, significantly promoting the fast

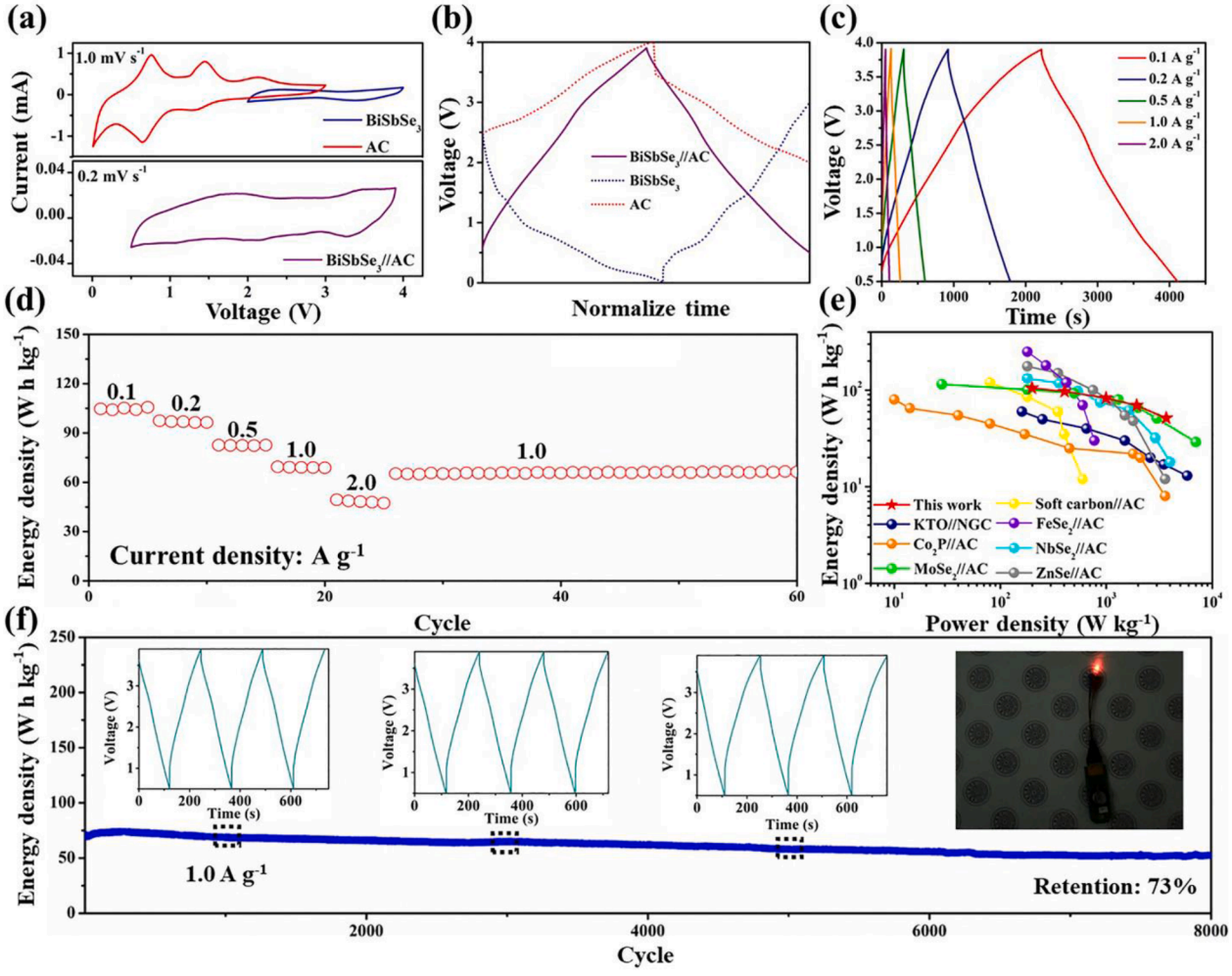

Fig. 9. (a) CV profiles of AC and $BiSbSe_3$ half cells (top) and a $BiSbSe_3$//AC PIHC (bottom). (b) Normalized charge/discharge curves of two half cells and a full cell. (c) Charge/discharge curves of the $BiSbSe_3$//AC PIHC at various current densities. (d) Rate performance of the $BiSbSe_3$//AC PIHC at current densities ranging from 0.1 to 2 A g^{-1}. (e) Ragone plots of the $BiSbSe_3$//AC PIHC compared with those of PIHCs. (f) Long-term cycling performance of the $BiSbSe_3$//AC PIHC. Insets present the pseudocapacitive profile of a $BiSbSe_3$//AC PIHC and a digital picture while lighting a LED bulb.

pseudocapacitive storage mechanism of $FeCN_2$@NC [56]. Therefore, it is speculated that the reversible intermediate phase of $K_3(Bi,Sb)Se_3$ has great potential for PIBs and promotes the good rate performance of $BiSbSe_3$. Next, the reversible intermediate phase of $K_3(Bi,Sb)Se_3$ is converted to metal (Bi,Sb) and K_2Se. The resulting metals (Bi,Sb) react with K^+ to form K-(Bi,Sb) alloys. Among the candidate materials for PIB anodes, conversion-alloy type materials have recently attracted considerable attention. These materials always have a high theoretical specific capacity and suitable working potential. Therefore, inspired by battery performance, kinetics, and mechanistic studies, $BiSbSe_3$ should be considered a promising anode material and further studied for application in PIBs and PIHCs.

Commercial AC was used as the cathode material to fabricate a PIHC device (denoted as $BiSbSe_3$//AC). In order to achieve high energy and power densities, the voltage window of the $BiSbSe_3$//AC should be in a voltage range of 0.5−3.9 V. Fig. 9a shows the CV curve of the successfully assembled PIHC. The small cathode peak around 3.5 V in the PIHC indicates a mixed charge storage mechanism of Faradaic and non-Faradaic reactions. The charge/discharge curves of the $BiSbSe_3$//potassium half-cell, AC//potassium half-cell and $BiSbSe_3$//AC full-cell are shown in Fig. 9b. Additionally, the CV curve, cycle performance and corresponding charge/discharge curves of the AC half cells deliver a specific capacity of 34 mA h g^{-1} at a current density of 50 mA g^{-1} (Fig. S28). Nearly linear charging/discharging curves indicate typical capacitor behavior, which is conducive to good rate performance. In addition, the charge/discharge curves of $BiSbSe_3$//AC under different current densities are shown in Fig. 9c. Notably, the high energy density of 105 Wh kg^{-1} operating at a current density of 100 mA g^{-1} for over 120 s (based on the total mass of AC and $BiSbSe_3$) is significantly higher than the vast majority of conventional potassium capacitors previously reported. When the current density is 0.1, 0.2, 0.5, 1 and 2 A g^{-1}, $BiSbSe_3$//AC still produces energy densities of 105, 97, 83, 69, and 51 W h kg^{-1}, equivalent to power densities of 199, 405, 995, 1,937, and 3,677 W kg^{-1}, respectively (Fig. 9d). When the current density is gradually returned to 1 A g^{-1}, the energy density can be restored to 69 W h kg^{-1}, showing excellent reversibility. In addition, $BiSbSe_3$//AC can easily drive light emitting diodes (LEDs) to emit light. Furthermore, kinetics analysis of $BiSbSe_3$//AC was carried out (Fig. S29). The peak current has no obvious overpotential shifting at high scan rates, indicating that the pseudocapacitive component of $BiSbSe_3$//AC is highly dominated. To evaluate the advantages of this novel PIHC, the energy and power densities of carbon-based and non-carbon-based PIHCs are plotted in a Ragone plots (Fig. 9e). The PIHC fabricated here shows the best power density when compared to previously reported $K_2Ti_6O_{13}$(KTO)//AC, Co_2P@rGO//AC, $MoSe_2$//AC, soft carbon//AC, $FeSe_2$//AC, $NbSe_2$//AC, and ZnSe//AC devices. As expected, a maximum energy density of 105 W h kg^{-1} can be achieved at a power density of 199 W kg^{-1}. Even at a high power density of 3,677 W kg^{-1}, the fabricated PIHC still maintains an energy density of 51 W h kg^{-1}, which is better than the previously reported $NbSe_2$//AC [57–63]. Importantly, $BiSbSe_3$//AC exhibits an ultra-long cycle performance (over 8,000 cycles) with a capacity retention of 73% at a high current density of 1 A g^{-1}, indicating its potential application as a high-performance energy storage device. In addition, the long-term cycling performance of $BiSbSe_3$//AC can even achieve 8000 cycles at 1000 mA g^{-1} with a capacity retention of 73%. The first, second, and third insets of Fig. 9f exhibit voltage curves at around 1,000, 3,000, and 5,000 cycles. Note that the similarly shaped of voltage curves are obtained, indicating extraordinary cycling stability and reversibility; the $BiSbSe_3$//AC can easily make a red LED shine (inset in Fig. 9f).

Additionally, a potassium-ion full battery with a $BiSbSe_3$ anode and PB cathode was constructed, and the test voltage ranged from 1 to 3.8 V to further investigate the application potential of the prepared $BiSbSe_3$. PB was synthesized via the coprecipitation method and all of the diffraction peaks of the prepared product were well identified as the crystal phase of $K_2Co[Fe(CN)_6]$ (PDF no. 31-1000) (Fig. S30). According to the charge/discharge curves, the PB cathode provides 57.8 mA h g^{-1} when the working voltage ranges from 2 to 4 V. Additionally, the CV curve, cycle performance and corresponding charge/discharge curves of the PB half cells delivered a specific capacity of 57.8 mA h g^{-1} at a current density of 120 mA g^{-1} (Fig. S31). In order to optimize the electrochemical performance of potassium ion full cell, the mass proportion of the anode: cathode had been adjusted to the ratios of 1:4.5. The $BiSbSe_3$//PB full battery was galvanostatically cycled at 100 mA g^{-1} in the voltage range of 1–3.8 V to obtain an average discharge voltage of 2.8 V. Fig. 10a shows the two main plateaus appearing in the blue curve, namely 3.3 V (charging plateaus) and 2.8. V (discharging plateaus). Fig. 10b shows the CV curve of the $BiSbSe_3$//PB full battery. After the first two cycles, the selected 3rd, 4th, and 5th curves overlap, indicating that the $BiSbSe_3$//PB full battery has good reversibility and stability. The rate performance of $BiSbSe_3$//PB full cell are shown in Fig. 10c, d. Fig. 10c shows the charge/discharge curves of $BiSbSe_3$//PB full cell under different current densities. The curves at different current densities have similar shapes, indicating good reversibility. When the current density is 0.1, 0.2, 0.4, 0.6, 0.8 and 1 A g^{-1}, the average discharge capacity of $BiSbSe_3$//PB full battery is 59.0, 56.6, 49.1, 45.0, 41.1 and 39.5 mA h g^{-1}, respectively. These values are usually equivalent to power densities of 202.9, 407.2, 805.8, 1198.0, 1581.9 and 1964.2 W kg^{-1}, respectively (Fig. 10e). When the current density returns to 0.1 A g^{-1}, the specific capacity quickly returns to 61.7 mA h g^{-1}. After the rate performance test, the $BiSbSe_3$//PB full battery was cycled at 500 mA g^{-1}. $BiSbSe_3$//PB delivers a discharge capacity of 40.0 mA h g^{-1} after 200 cycles, shows excellent cycle performance and rate performance. Interestingly, the full battery can light up a red LED after being fully charged (Fig. 10d). The electrochemical performance of $BiSbSe_3$//PB was compared with the reported literature results of potassium ion full cell [20,41,54,64-71]. The battery capacity based on the total mass of anode and cathode materials and operating voltage is shown in Fig. 10f. $BiSbSe_3$//PB has a relatively high working voltage and high energy density. Notably, the excellent performance of the $BiSbSe_3$//PB full cells is consistent with the contribution of K^+ storage in half cells. The above results demonstrate that the $BiSbSe_3$ electrode is a very promising anode for application of future PIBs and PIHCs.

3. Conclusion

We have shown that the ternary $Bi_{2-x}Sb_xSe_3$ system prepared through a solid solution mechanism with a whole composition range can result in a high-efficiency PIB anode. When $x \geq 1$, the bond breaking and elongation accompanying the structural transition were found to effectively soften the chemical bonds, preventing volume change that leads to material pulverization during cycling. Furthermore, the phase evolution process of $BiSbSe_3$ during discharge/charge was determined by first-principle calculations, *in-situ* XRD and *ex-situ* TEM analyses. Notably, the formation of the quaternary mesophase of $K_3(Bi,Sb)Se_3$ was found to play a very important role in the electrochemical reaction that ensures that $Bi_{2-x}Sb_xSe_3$ undergoes a highly reversible potassiation/depotassiation reaction and achieves high performance. Excellent electrochemical performance of a $BiSbSe_3$ anode for a PIB with highly reversible potassium storage capacity was shown. In addition, the $BiSbSe_3$ electrode not only exhibited very low resistance after 10 cycles but also enhanced pseudocapacitive performance to allow rapid chemical kinetics to high-performance potassium-ion storage. Importantly, the PIHC demonstration of $BiSbSe_3$ materials exhibiting high voltage PIB full cells and high energy density show that $BiSbSe_3$ can be a satisfactory bi-functional electrode material. Overall, the strategy of exploiting composition-induced chemical bond softening and intermediate phase opens a new avenue for existing potassium-ion anode materials. It also enables those compounds that originally performed poorly under their binary system to improve their performance under ternary chemical composition regulation. We believe that this research can facilitate the realization and conceptual expansion of ternary or multi-element

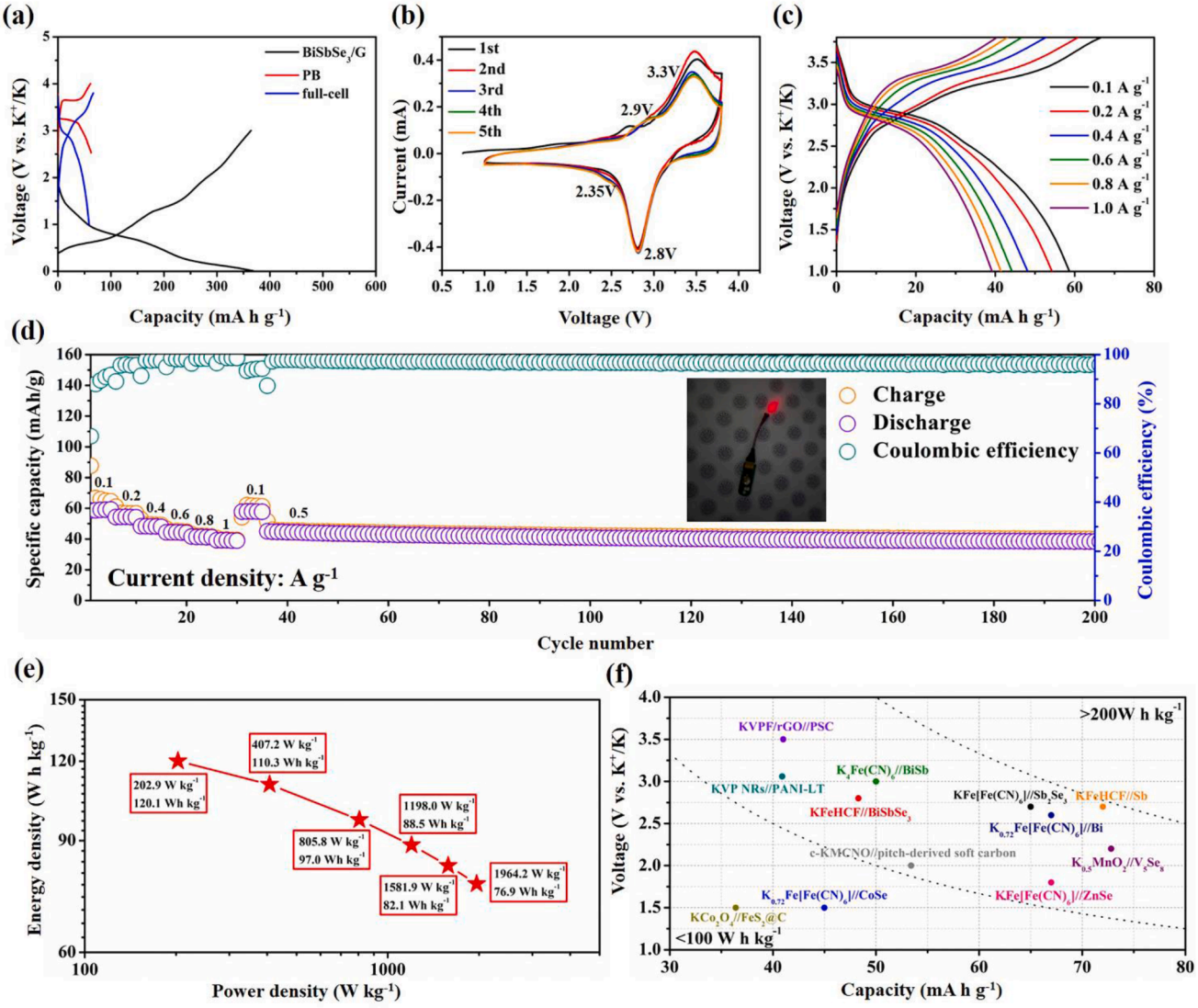

Fig. 10. (a) Charge/discharge curves of PB and $BiSbSe_3$ half cells and a $BiSbSe_3$//PB full cell. (b) CV profiles of the $BiSbSe_3$//PB full cell. (c) The charge–discharge profiles of $BiSbSe_3$//PB full cell at rates increased from 0.1 to 1 A g^{-1}. (d) Rate performance of the $BiSbSe_3$//PB full cell at current densities ranging from 0.1 to 1 A g^{-1} and cycling stability at 0.5 A g^{-1}. The inset shows a digital picture of the LED lighting test. (e) Corresponding energy densities and power densities in Ragone plots. (f) Comparison of the electrochemical performances.

materials in multidisciplinary material science and electrochemical reactions for next-generation potassium-ion storage systems.

CRediT authorship contribution statement

Wei-Cheng Lin: Conceptualization, Methodology, Data curation. **Yi-Chun Yang:** Methodology, Data curation. **Hsing-Yu Tuan:** Conceptualization, Resources, Supervision, Writing – review & editing.

Declaration of Competing Interest

The authors declare that they have no known competing financial interests or personal relationships that could have appeared to influence the work reported in this paper.

Acknowledgments

This work was supported by 2030 Cross-Generation Young Scholars Program by the Ministry of Science and Technology, Taiwan (MOST 111-2628-E-007-008). H.-Y. Tuan also acknowledges financial support from the National Tsing Hua University, Taiwan, through the grant of 109QI030E1.

Supplementary materials

Supplementary material associated with this article can be found, in the online version, at doi:10.1016/j.ensm.2022.06.010.

References

[1] J. Wang, L. Fan, Z. Liu, S. Chen, Q. Zhang, L. Wang, H. Yang, X. Yu, B. Lu, In situ alloying strategy for exceptional potassium ion batteries, ACS Nano 13 (2019) 3703–3713.
[2] L.A. Selis, J.M. Seminario, Dendrite formation in silicon anodes of lithium-ion batteries, RSC Adv. 8 (2018) 5255–5267.
[3] K.-W. Tseng, S.-B. Huang, W.-C. Chang, H.-Y. Tuan, Synthesis of mesoporous germanium phosphide microspheres for high-performance lithium-ion and sodium-ion battery anodes, Chem. Mater. 30 (2018) 4440–4447.
[4] K.-T. Chen, Y.-C. Yang, L.-M. Lyu, M.-Y. Lu, H.-Y. Tuan, situ formed robust submicron-sized nanocrystalline aggregates enable highly-reversible potassium ion storage, Nano Energy 88 (2021), 106233.
[5] G. Chen, Y. Bai, Y. Gao, F. Wu, C Wu, Chalcogenide electrolytes for all-solid-state sodium ion batteries, Acta Phys. Chim. Sin. 36 (2020).

[6] Y.-Y. Hsieh, K.-T. Chen, H.-Y. Tuan, A synergetic SnSb-amorphous carbon composites prepared from polyesterification process as an ultrastable potassium-ion battery anode, Chem. Eng. J. 420 (2021), 130451.

[7] L. Fan, R. Ma, Q. Zhang, X. Jia, B. Lu, Graphite anode for a potassium-ion battery with unprecedented performance, Angew. Chem. Int. Ed. 131 (2019) 10610–10615.

[8] Z. Yan, M. Obrovac, Quantifying the cost effectiveness of non-aqueous potassium-ion batteries, J. Power Sources 464 (2020), 228228.

[9] T. Wang, D. Shen, H. Liu, H. Chen, Q. Liu, B. Lu, A Sb_2S_3 nanoflower/MXene composite as an anode for potassium-ion batteries, ACS Appl. Mater. Interfaces 12 (2020) 57907–57915.

[10] R. Hu, K. Zhu, K. Ye, J. Yan, Q. Wang, D. Cao, G. Wang, Influence of potential range selection on the SnS@ C/rGO anodes in potassium ion battery, Appl. Surf. Sci. 536 (2021), 147832.

[11] T. Yang, J. Liu, D. Yang, Q. Mao, J. Zhong, Y. Yuan, X. Li, X. Zheng, Z. Ji, H. Liu, Bi_2Se_3@ C rod-like architecture with outstanding electrochemical properties in lithium/potassium-ion batteries, ACS Appl. Energy Mater. 3 (2020) 11073–11081.

[12] C. Shen, G. Song, X. Zhu, D. Wang, L. Huang, Z. Sun, Y. Wu, An in-depth study of heteroatom boosted anode for potassium-ion batteries, Nano Energy 78 (2020), 105294.

[13] S. Wang, P. Xiong, X. Guo, J. Zhang, X. Gao, F. Zhang, X. Tang, P.H. Notten, G. Wang, A stable conversion and alloying anode for potassium-ion batteries: a combined strategy of encapsulation and confinement, Adv. Funct. Mater. 30 (2020), 2001588.

[14] R. Verma, P.N. Didwal, A.-G. Nguyen, C.-J. Park, SnSe nanocomposite chemically-bonded with carbon-coating as an anode material for K-ion batteries with outstanding capacity and cyclability, Chem. Eng. J. 421 (2021), 129988.

[15] A. Eftekhari, The rise of lithium–selenium batteries, Sustain. Energy Fuels 1 (2017) 14–29.

[16] C.A. Etogo, H. Huang, H. Hong, G. Liu, L. Zhang, Metal–organic-frameworks-engaged formation of $Co_{0.85}Se$@ C nanoboxes embedded in carbon nanofibers film for enhanced potassium-ion storage, Energy Stor. Mater. 24 (2020) 167–176.

[17] W. Wang, B. Jiang, C. Qian, F. Lv, J. Feng, J. Zhou, K. Wang, C. Yang, Y. Yang, S. Guo, Pistachio-shuck-like $MoSe_2$/C core/shell nanostructures for high-performance potassium-ion storage, Adv. Mater. 30 (2018), 1801812.

[18] Y. Liu, C. Yang, Y. Li, F. Zheng, Y. Li, Q. Deng, W. Zhong, G. Wang, T. Liu, $FeSe_2$/nitrogen-doped carbon as anode material for potassium-ion batteries, Chem. Eng. J. 393 (2020), 124590.

[19] Q. Yu, B. Jiang, J. Hu, C.Y. Lao, Y. Gao, P. Li, Z. Liu, G. Suo, D. He, W. Wang, Metallic octahedral $CoSe_2$ threaded by N-doped carbon nanotubes: a flexible framework for high-performance potassium-ion batteries, Adv. Sci. 5 (2018), 1800782.

[20] C. Yang, F. Lv, K. Dong, F. Lai, K. Zhao, F. Sun, S. Dou, Q. Wang, J. Xu, P. Zhang, Carbon-coated ultrathin metallic V_5Se_8 nanosheet for high-energy-density and robust potassium storage, Energy Storage Mater. 35 (2021) 1–11.

[21] H. Lin, M. Li, X. Yang, D. Yu, Y. Zeng, C. Wang, G. Chen, F. Du, Nanosheets-assembled CuSe crystal pillar as a stable and high-power anode for sodium-ion and potassium-ion batteries, Adv. Energy Mater. 9 (2019), 1900323.

[22] C. Yang, J. Feng, F. Lv, J. Zhou, C. Lin, K. Wang, Y. Zhang, Y. Yang, W. Wang, J. Li, Metallic graphene-like VSe_2 ultrathin nanosheets: superior potassium-ion storage and their working mechanism, Adv. Mater. 30 (2018), 1800036.

[23] L. Zhang, H. Li, T. Sheng, J. Chen, M. Lu, Y. Xu, H. Yuan, J. Zhao, J. Lu, Synthesizing Cu-doped $CoSe_2$ nanoframe cubics for Na-ion batteries electrodes, Colloids Surf. A Physicochem. Eng. Asp. 628 (2021), 127379.

[24] K. Zhang, M. Park, L. Zhou, G.H. Lee, J. Shin, Z. Hu, S.L. Chou, J. Chen, Y.M. Kang, Cobalt-doped FeS_2 nanospheres with complete solid solubility as a high-performance anode material for sodium-ion batteries, Angew. Chem. Int. Ed. 55 (2016) 12822–12826.

[25] Y. Feng, M. Xu, T. He, B. Chen, F. Gu, L. Zu, R. Meng, J. Yang, CoPSe: a new ternary anode material for stable and high-rate sodium/potassium-ion batteries, Adv. Mater. 33 (2021), 2007262.

[26] Z. Wu, G. Liang, J. Wu, W.K. Pang, F. Yang, L. Chen, B. Johannessen, Z. Guo, Synchrotron x-ray absorption spectroscopy and electrochemical study of Bi_2O_2Se electrode for lithium-/potassium-ion storage, Adv. Energy Mater. 11 (2021), 2100185.

[27] Y. Long, J. Yang, X. Gao, X. Xu, W. Fan, J. Yang, S. Hou, Y. Qian, Solid-solution anion-enhanced electrochemical performances of metal sulfides/selenides for sodium-ion capacitors: the case of $FeS_{2-x}Se_x$, ACS Appl. Mater. Interfaces 10 (2018) 10945–10954.

[28] R. Yokozaki, H. Kobayashi, T. Mandai, I. Honma, Application of spinel $MgMn_{2-x}Al_xO_4$ as cathode for Mg rechargeable battery, in: ECS Meeting Abstracts, IOP Publishing, 2020, p. 3473.

[29] H. Bhatia, D.T. Thieu, A.H. Pohl, V.S.K. Chakravadhanula, M.H. Fawey, C. Kübel, M. Fichtner, Conductivity optimization of tysonite-type $La_{1-x}Ba_xF_{3-x}$ solid electrolytes for advanced fluoride ion battery, ACS Appl. Mater. Interfaces 9 (2017) 23707–23715.

[30] H. Konishi, T. Minato, T. Abe, Z. Ogumi, Electrochemical reaction mechanism for $Bi_{1-x}Ba_xF_{3-x}$ (x= 0, 0.1, 0.2, and 0.4) electrodes in lithium-ion batteries, Chemistryselect 2 (2017) 6399–6406.

[31] T. Kyratsi, E. Hatzikraniotis, M. Paraskevopoulous, J.S. Dyck, H. Shin, C. Uher, M. G. Kanatzidis, Lattice thermal conductivity of $K_2(Bi_{1-z}Sb_z)_8Se_{13}$ solid solutions, J. Appl. Phys. 95 (2004) 4140–4146.

[32] J. Wang, B. Wang, Z. Liu, L. Fan, Q. Zhang, H. Ding, L. Wang, H. Yang, X. Yu, B. Lu, Nature of bimetallic oxide Sb_2MoO_6/rGO anode for high-performance potassium-ion batteries, Adv. Sci. 6 (2019), 1900904.

[33] S. Guo, H. Li, Y. Lu, Z. Liu, X. Hu, Lattice softening enables highly reversible sodium storage in anti-pulverization Bi–Sb alloy/carbon nanofibers, Energy Storage Mater. 27 (2020) 270–278.

[34] S. Wang, Y. Sun, J. Yang, B. Duan, L. Wu, W. Zhang, J. Yang, High thermoelectric performance in Te-free $(Bi, Sb)_2Se_3$ via structural transition induced band convergence and chemical bond softening, Energy Environ. Sci. 9 (2016) 3436–3447.

[35] K.-T. Chen, S. Chong, L. Yuan, Y.-C. Yang, H.-Y. Tuan, Conversion-alloying dual mechanism anode: nitrogen-doped carbon-coated Bi_2Se_3 wrapped with graphene for superior potassium-ion storage, Energy Storage Mater. 39 (2021) 239–249.

[36] Z. Yang, W. Li, G. Zhang, J. Wang, J. Zuo, Q. Xu, H. Shan, X. He, M. Lv, J. Hu, Constructing SbOC bond to improve the alloying reaction reversibility of free-standing Sb2Se3 nanorods for potassium-ion batteries, Nano Energy 93 (2022), 106764.

[37] Y. Du, Z. Yi, Z. Zhang, J. Liao, Y. Xu, J. Bao, X. Zhou, A highly stable potassium-ion battery anode enabled by multilayer graphene sheets embedded with SnTe nanoparticles, Chem. Eng. J. 435 (2022), 135100.

[38] B. Sheng, L. Wang, H. Huang, H. Yang, R. Xu, X. Wu, Y. Yu, Boosting potassium storage by integration advantageous of defect engineering and spatial confinement: a case study of Sb_2Se_3, Small 16 (2020), 2005272.

[39] K.-T. Chen, H.-Y. Tuan, Bi–Sb nanocrystals embedded in phosphorus as high-performance potassium ion battery electrodes, ACS Nano 14 (2020) 11648–11661.

[40] Q. Wu, B. Chen, H. Xie, X. Bai, M. Liang, Z. Wu, X. Jin, C. He, N. Zhao, Bismuth-antimony alloy nanoparticles encapsulated in 3D carbon framework: synergistic effect for enhancing interfacial potassium storage, Chem. Eng. J. 430 (2022), 132906.

[41] P. Xiong, J. Wu, M. Zhou, Y. Xu, Bismuth–antimony alloy nanoparticle@ porous carbon nanosheet composite anode for high-performance potassium-ion batteries, ACS Nano 14 (2019) 1018–1026.

[42] Z. Yi, Y. Qian, S. Jiang, Y. Li, N. Lin, Y. Qian, Self-wrinkled graphene as a mechanical buffer: a rational design to boost the K-ion storage performance of Sb_2Se_3 nanoparticles, Chem. Eng. J. 379 (2020), 122352.

[43] N. Hussain, M. Li, B. Tian, H. Wang, Co_3Se_4 quantum dots as an ultrastable host material for potassium-ion intercalation, Adv. Mater. 33 (2021), 2102164.

[44] H. Wu, S. Lu, S. Xu, J. Zhao, Y. Wang, C. Huang, A. Abdelkader, W.A. Wang, K. Xi, Y. Guo, Blowing iron chalcogenides into two-dimensional flaky hybrids with superior cyclability and rate capability for potassium-ion batteries, ACS Nano 15 (2021) 2506–2519.

[45] Z. Xia, X. Chen, H. Ci, Z. Fan, Y. Yi, W. Yin, N. Wei, J. Cai, Y. Zhang, J. Sun, Designing N-doped graphene/$ReSe_2$/Ti_3C_2 MXene heterostructure frameworks as promising anodes for high-rate potassium-ion batteries, J. Energy Chem. 53 (2021) 155–162.

[46] D. Xu, L. Chen, X. Su, H. Jiang, C. Lian, H. Liu, L. Chen, Y. Hu, H. Jiang, C. Li, Heterogeneous $MoSe_2$/nitrogen-doped-carbon nanoarrays: engineering atomic interface for potassium-ion storage, Adv. Funct. Mater. (2021), 2110223.

[47] L. Xu, W. Guo, L. Zeng, X. Xia, Y. Wang, P. Xiong, Q. Chen, J. Zhang, M. Wei, Q. Qian, V_3Se_4 embedded within N/P co-doped carbon fibers for sodium/potassium ion batteries, Chem. Eng. J. 419 (2021), 129607.

[48] C.-Y. Tsai, C.-H. Chang, T.-L. Kao, K.-T. Chen, H.-Y. Tuan, Shape matters: $SnP_{0.94}$ teardrop nanorods with boosted performance for potassium ion storage, Chem. Eng. J. 417 (2021), 128552.

[49] S.-C. Lu, M.-C. Hsiao, M. Yorulmaz, L.-Y. Wang, P.-Y. Yang, S. Link, W.-S. Chang, H.-Y. Tuan, Single-crystalline copper nano-octahedra, Chem. Mater. 27 (2015) 8185–8188.

[50] J. Tang, C.-Y. Wang, F. Xiu, A.J. Hong, S. Chen, M. Wang, C. Zeng, H.-J. Yang, H.-Y. Tuan, C.-J. Tsai, Single-crystalline Ni_2Ge/Ge/Ni_2Ge nanowire heterostructure transistors, Nanotechnology 21 (2010), 505704.

[51] S.-H. Chang, B.-C. Chiu, T.-L. Gao, S.-L. Jheng, H.-Y. Tuan, Selective synthesis of copper gallium sulfide ($CuGaS_2$) nanostructures of different sizes, crystal phases, and morphologies, CrystEngComm 16 (2014) 3323–3330.

[52] J. Wang, B. Wang, B. Lu, Nature of novel 2D van der Waals heterostructures for superior potassium ion batteries, Adv. Energy Mater. 10 (2020), 2000884.

[53] C.-H. Chang, K.-T. Chen, Y.-Y. Hsieh, C.-B. Chang, H.-Y. Tuan, Crystal facet and architecture engineering of metal oxide nanonetwork anodes for high-performance potassium ion batteries and hybrid capacitors, ACS Nano (2022).

[54] L. Guo, L. Cao, J. Huang, J. Li, K. Kajiyoshi, J. He, H. Qi, Guiding fabrication of continuous carbon-confined Sb_2Se_3 nanoparticle structure for durable potassium-storage performance, ACS Appl. Energy Mater. 4 (2021) 10391–10403.

[55] B. Li, Z. He, J. Zhao, W. Liu, Y. Feng, J. Song, Advanced Se_3P_4@ C anode with exceptional cycling life for high performance potassium-ion batteries, Small 16 (2020), 1906595.

[56] H. Qi, C. Zhao, J. Huang, C. He, L. Tang, W. Deng, Metastable $FeCN_2$@ nitrogen-doped carbon with high pseudocapacitance as an anode material for sodium ion batteries, Nanoscale (2022).

[57] M. Chen, L. Wang, X. Sheng, T. Wang, J. Zhou, S. Li, X. Shen, M. Zhang, Q. Zhang, X. Yu, An ultrastable nonaqueous potassium-ion hybrid capacitor, Adv. Funct. Mater. 30 (2020), 2004247.

[58] J. Ge, B. Wang, J. Wang, Q. Zhang, B. Lu, Nature of $FeSe_2$/N-C anode for high performance potassium ion hybrid capacitor, Adv. Energy Mater. 10 (2020), 1903277.

[59] J. Ruan, J. Zang, J. Hu, R. Che, F. Fang, F. Wang, Y. Song, D. Sun, Respective roles of inner and outer carbon in boosting the K^+ storage performance of dual-carbon-confined ZnSe, Adv. Sci. (2021), 2104822.

[60] S. Dong, Z. Li, Z. Xing, X. Wu, X. Ji, X. Zhang, Novel potassium-ion hybrid capacitor based on an anode of $K_2Ti_6O_{13}$ microscaffolds, ACS Appl. Mater. Interfaces 10 (2018) 15542–15547.

[61] Y. Yi, Z. Sun, C. Li, Z. Tian, C. Lu, Y. Shao, J. Li, J. Sun, Z. Liu, Designing 3D biomorphic nitrogen-doped $MoSe_2$/graphene composites toward high-performance potassium-ion capacitors, Adv. Funct. Mater. 30 (2020), 1903878.
[62] Y. Wang, Z. Zhang, G. Wang, X. Yang, Y. Sui, F. Du, B. Zou, Ultrafine Co_2P nanorods wrapped by graphene enable a long cycle life performance for a hybrid potassium-ion capacitor, Nanoscale Horiz. 4 (2019) 1394–1401.
[63] Y. Luo, L. Liu, K. Lei, J. Shi, G. Xu, F. Li, J. Chen, A nonaqueous potassium-ion hybrid capacitor enabled by two-dimensional diffusion pathways of dipotassium terephthalate, Chem. Sci. 10 (2019) 2048–2052.
[64] K. Lei, C. Wang, L. Liu, Y. Luo, C. Mu, F. Li, J. Chen, A porous network of bismuth used as the anode material for high-energy-density potassium-ion batteries, Angew. Chem. Int. Ed. 130 (2018) 4777–4781.
[65] Y. Liu, Q. Deng, Y. Li, Y. Li, W. Zhong, J. Hu, X. Ji, C. Yang, Z. Lin, K. Huang, CoSe@ N-doped carbon nanotubes as a potassium-ion battery anode with high initial coulombic efficiency and superior capacity retention, ACS Nano 15 (2021) 1121–1132.
[66] S. Liang, Z. Yu, T. Ma, H. Shi, Q. Wu, L. Ci, Y. Tong, J. Wang, Z. Xu, Mechanistic insights into the structural modulation of transition metal selenides to boost potassium ion storage stability, ACS Nano 15 (2021) 14697–14708.
[67] X.-D. He, Z.-H. Liu, J.-Y. Liao, X. Ding, Q. Hu, L.-N. Xiao, S. Wang, C.-H. Chen, A three-dimensional macroporous antimony@ carbon composite as a high-performance anode material for potassium-ion batteries, J. Mater. Chem. A 7 (2019) 9629–9637.
[68] J. Liao, C. Chen, Q. Hu, Y. Du, Y. He, Y. Xu, Z. Zhang, X. Zhou, A low-strain phosphate cathode for high-rate and ultralong cycle-life potassium-ion batteries, Angew. Chem. Int. Ed. 60 (2021) 25575–25582.
[69] L. Duan, Y. Xu, Z. Zhang, J. Xu, J. Liao, J. Xu, Y. Sun, Y. He, X. Zhou, A high-performance cathode for potassium-ion batteries based on uniform P3-type $K_{0.5}Mn_{0.8}Co_{0.1}Ni_{0.1}O_2$ porous microcuboids, J. Mater. Chem. A 9 (2021) 22820–22826.
[70] J.Liao Xu, Y. Xu, J. Li, C. Zhu, J. Lin, X. Zhou, Facile synthesis of $KVPO_4F$/reduced graphene oxide hybrid as a high-performance cathode material for potassium-ion batteries, J. Energy Chem. 68 (2022) 284–292.
[71] Y. Du, W. Weng, Z. Zhang, Y. He, J. Xu, J. Sun, J. Liao, J. Bao, X. Zhou, Candied-haws-like architecture consisting of FeS_2@ C core–shell particles for efficient potassium storage, ACS Mater. Lett. 3 (2021) 356–363.